

Improving Performance, Robustness, and Fairness of Radiographic AI Models with Finely-Controllable Synthetic Data

Stefania L. Moroiu^{1,3,*}, Christian Bluethgen^{1,5}, Pierre Chambon¹, Mehdi Cherti^{6,7}, Jean-Benoit Delbrouck^{1,2}, Magdalini Paschali^{1,2}, Brandon Price^{8,9}, Judy Gichoya⁸, Jenia Jitsev^{6,7}, Curtis P. Langlotz^{1,2}, Akshay S. Chaudhari^{1,2,4}

¹ Center for Artificial Intelligence in Medicine and Imaging, Stanford University. ² Department of Radiology, Stanford University. ³ Department of Applied Physics, Stanford University. ⁴ Department of Biomedical Data Science, Stanford University. ⁵ Institute for Diagnostic and Interventional Radiology, University Hospital Zurich, University of Zurich. ⁶ LAION. ⁷ Juelich Supercomputing Center (JSC), Research Center Juelich (FZJ). ⁸ Department of Radiology & Imaging Sciences, Emory University. ⁹ Department of Radiology, University of Florida College of Medicine.

Achieving robust performance and fairness across diverse patient populations remains a central challenge in developing clinically deployable deep learning models for diagnostic imaging. Synthetic data generation has emerged as a promising strategy to address current limitations in dataset scale and diversity. In this study, we introduce RoentGen-v2, a state-of-the-art text-to-image diffusion model for chest radiographs that enables fine-grained control over both radiographic findings and patient demographic attributes, including sex, age, and race/ethnicity. RoentGen-v2 is the first model to generate clinically plausible chest radiographs with explicit demographic conditioning, facilitating the creation of a large, demographically balanced synthetic dataset comprising over 565,000 images. We use this large synthetic dataset to evaluate optimal training pipelines for downstream disease classification models. In contrast to prior work that combines real and synthetic data naively, we propose an improved training strategy that leverages synthetic data for supervised pretraining, followed by fine-tuning on real data. Through extensive evaluation on over 137,000 held-out chest radiographs from five institutions, we demonstrate that synthetic pretraining consistently improves model performance, generalization to out-of-distribution settings, and fairness across demographic subgroups defined across varying fairness metrics. Across datasets, synthetic pretraining led to a 6.5% accuracy increase in the performance of downstream classification models, compared to a modest 2.7% increase when naively combining real and synthetic data. We observe this performance improvement simultaneously with the reduction of the underdiagnosis fairness gap by 19.3%, with marked improvements across intersectional subgroups of sex, age, and race/ethnicity. Our proposed data-centric training approach that combines high-fidelity synthetic training data with multi-stage training pipelines is label-efficient, reducing reliance on large quantities of annotated real data. These results highlight the potential of demographically controllable synthetic imaging to advance equitable and generalizable medical deep learning under real-world data constraints. We open source our code, trained models, and synthetic dataset at <https://github.com/StanfordMIMI/RoentGen-v2>.

* Corresponding author: slmoro@stanford.edu

1 Introduction

Chest radiography (CXR) is the most frequently performed medical imaging exam worldwide, playing a central role in both diagnostic workflows and routine screening. An estimated 2 billion CXR exams are acquired globally each year [1], including over 70 million in the United States [2]. Given this large volume of CXR studies and the global shortage of radiologists, deep learning models have emerged as promising tools to support radiographic interpretation [3]. Such models have demonstrated strong performance across a wide range of tasks, including disease classification [4–7], worklist prioritization [8], visual grounding [9, 10], and automatic report generation [11–13], with many systems obtaining regulatory clearances [14]. Despite these initial successes, several shortcomings remain that limit the translation of deep learning models into routine clinical practice. A major concern is the lack of generalizability: models trained on data from one institution often exhibit degraded performance when applied to external sites or new patient populations [15, 16]. Moreover, fairness concerns arise when models exhibit performance discrepancies across demographic subgroups, potentially contributing to inequitable clinical care [17–19]. Although fairness-aware training strategies have been proposed, these approaches often fail to generalize on out-of-distribution data and can come at the cost of reduced overall performance [20]. Currently, one of the most reliable approaches to improving both performance and fairness involves scaling the size and diversity of training datasets to better represent all patient demographic subgroups [17]. However, privacy regulations and institutional barriers limit the feasibility of aggregating large, multi-site datasets, and such efforts have seen limited success to date. These challenges highlight the need for novel methods that can enhance model performance and fairness simultaneously, while operating within real-world constraints on data availability and sharing.

Recent advances in generative diffusion models have significantly expanded the capabilities of deep learning in medical imaging [21, 22]. Text-to-image models such as RoentGen [23] and Cheff [24] have shown strong performance in synthesizing realistic CXRs with fine-grained control over disease-specific visual features. However, prior works leveraging diffusion-based synthetic data for CXR classification have several limitations. Thus far, conditioning has been limited to textual prompts describing radiographic findings, with little or no ability to control for demographic attributes such as age, sex, or race/ethnicity. This is a critical gap, given that computer vision models have been shown to detect and rely on demographic features, both explicitly and implicitly, when making predictions [25]. Consequently, the lack of demographic conditioning in earlier synthetic datasets limits their utility for studying or mitigating fairness-related concerns. Furthermore, while synthetic data augmentation has been shown to improve model performance both in-distribution and on external test sets [26, 27], the optimal strategies for integrating synthetic data into model development pipelines remain unclear. Open questions persist around building data-centric pipelines for ensuring fidelity and relevance of synthetic samples for specific downstream clinical tasks, and how to best combine synthetic and real data.

In this work, we hypothesized that diffusion models with text and demographic conditioning can be used to generate large-scale synthetic CXR datasets with balanced representation across demographic subgroups, thereby enabling more equitable and generalizable training for downstream disease classification tasks. We further investigated how synthetic data should best be integrated into disease classifier development pipelines, specifically whether supervised pretraining on synthetic images is more effective than using synthetic data for augmentation during task-specific training. Pretraining on diverse synthetic data has the potential to support the learning of robust, demographically invariant representations, thereby improving both performance and fairness across populations.

Our study makes four key contributions (Figure 1). First, we introduce RoentGen-v2, a state-of-the-art text-to-image diffusion model for CXRs, capable of high-fidelity image generation, with conditioning not only on radiographic findings but also on structured patient metadata, including sex, age, and race/ethnicity. Second, we used RoentGen-v2 to create a large, demographically balanced synthetic dataset comprising over 565,000 images. To ensure instruction-following of conditioning criteria, we integrated a quality control module into the generation pipeline that automatically filtered out inconsistent samples. Third, we conducted a comprehensive comparison of how synthetic data can be used to train disease classifiers, evaluating four strategies: (i) Using only real CXRs; (ii) Using only synthetic CXRs generated by RoentGen-v2; (iii) Augmenting real CXRs with synthetic CXRs as is common in the literature; (iv) A two-stage data-centric training, where we first perform

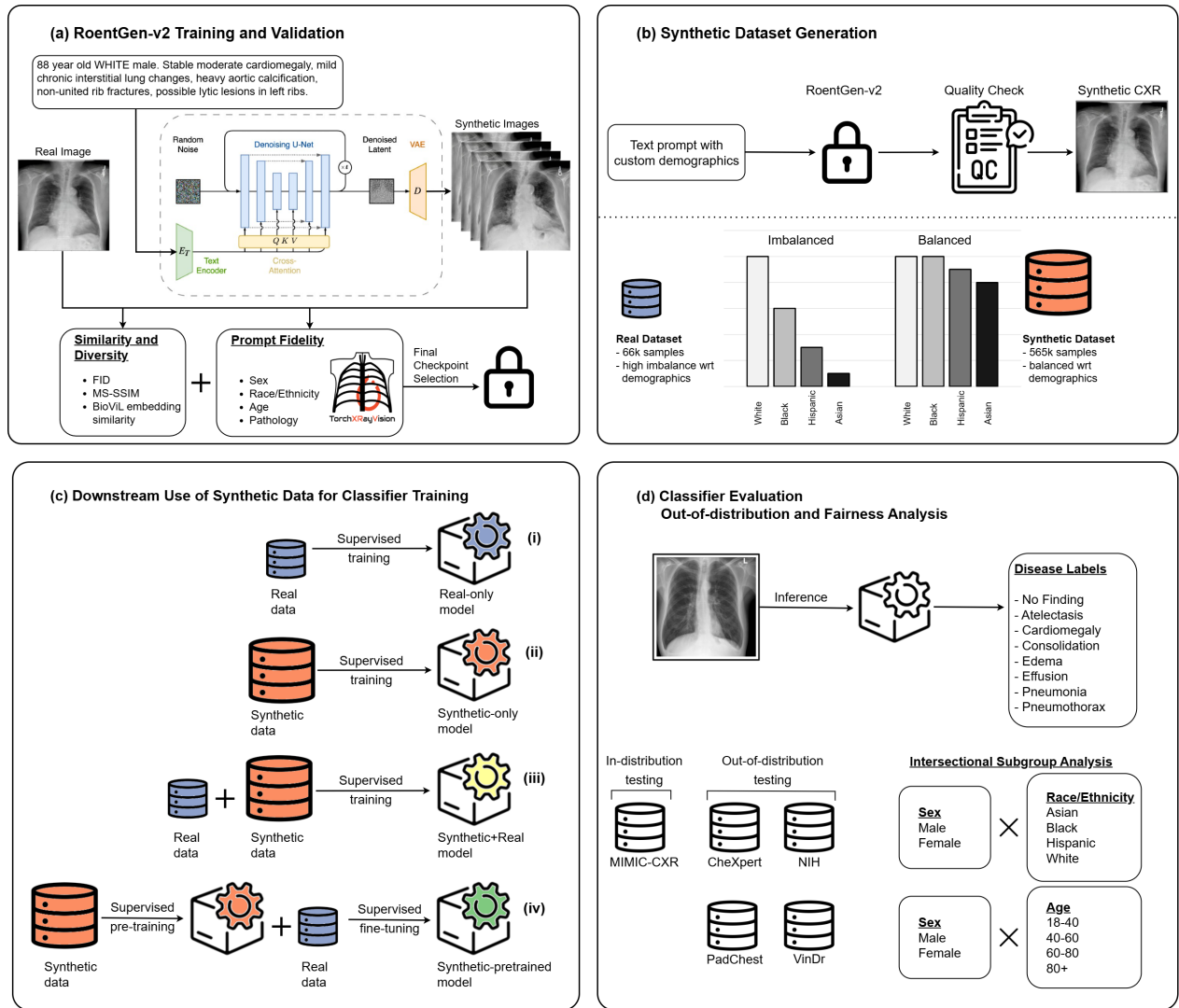


Figure 1 | Overview of the experimental approach. (a) RoentGen-v2 is created by fine-tuning Stable Diffusion v2.1 on real chest radiographs (CXRs), using radiology report text enriched with demographic information. (b) Top: A synthetic CXR dataset is generated by prompting the trained RoentGen-v2 model with customized prompts, followed by quality control. Bottom: Comparison between the real training dataset and the generated synthetic dataset. (c) Classification models are trained using four approaches: (i) Using only real CXRs; (ii) Using only synthetic CXRs generated by RoentGen-v2 ; (iii) Augmenting real CXRs with synthetic CXRs; (iv) Two-stage training, where we first perform supervised pretraining with synthetic CXRs, followed by fine-tuning on real CXRs. (d) The resulting classifiers are evaluated on multi-label classification tasks using both in-distribution and four out-of-distribution datasets, followed by intersectional subgroup analysis across sex, age, and race/ethnicity groups.

supervised pretraining with synthetic CXRs, followed by fine-tuning on real CXRs. Fourth, through systematic evaluation across five international datasets, we demonstrate that our two-stage supervised pretraining with synthetic data significantly improves both classification performance and fairness metrics across demographic subgroups. This approach consistently outperformed the other three training techniques.

Collectively, our findings show that high-quality, demographically controllable synthetic data are a powerful tool for improving performance and fairness in medical imaging deep learning, particularly in settings where real-world data are imbalanced, limited, or challenging to access. We open source RoentGen-v2 weights, our synthetic dataset, and corresponding code to facilitate future research.

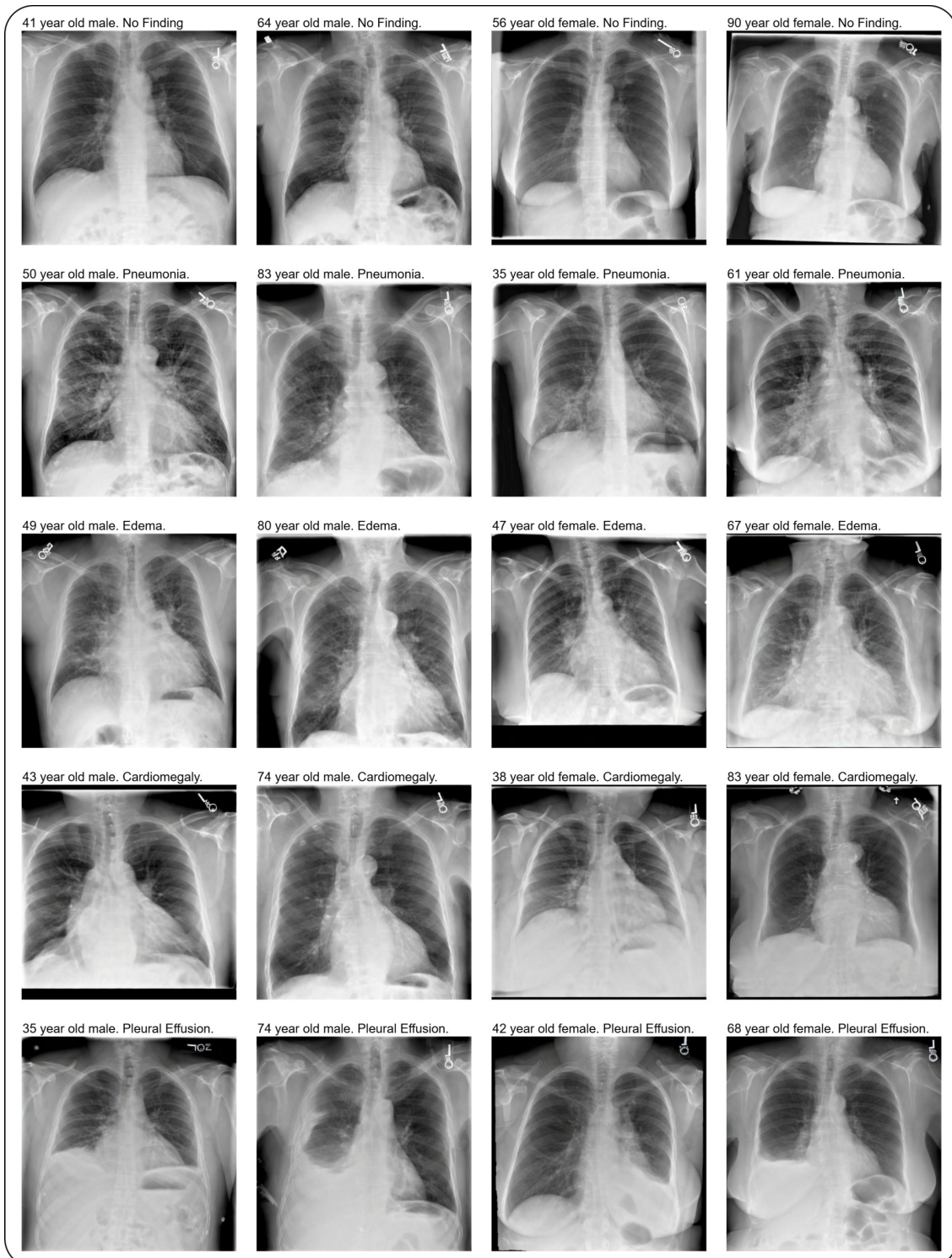


Figure 2 | Example synthetic chest radiographs (CXRs) conditioned on radiographic findings and demographic information. Each row displays a distinct radiographic finding: No Finding, Pneumonia, Edema, Cardiomegaly and Pleural Effusion. Columns demonstrate variation across sex and age groups. The generated images maintain high fidelity and accurately follow the conditioning text prompts.

2 Results

2.1 Generative Model with Demographic Conditioning

In this work, we present RoentGen-v2, which can condition image generation not only on radiographic findings, but also on patient demographic attributes (sex, age, race/ethnicity). Compared to the original RoentGen [23] model, we use a $\sim 2\times$ larger training dataset and use an improved baseline Stable Diffusion model (version 2.1 compared to version 1.4) to allow demographic-based metadata conditioning. We create a $16\times$ larger and demographically-balanced synthetic dataset (565,154 studies) to further rigorously evaluate data-centric approaches for best using synthetic data for training downstream classifiers with high accuracy, generalizability, and fairness. RoentGen-v2 was trained on a curated subset of the MIMIC-CXR [28] dataset for which images, radiology reports and patient metadata were available. We used the impression section, a summary section of a radiology report focused on the relevant findings and their interpretation. We incorporated demographic information in the text prompt following the structure `<AGE> year old <RACE> <SEX>. <IMPRESSION>`. RoentGen-v2 was trained on a total of 68k CXR-report pairs, compared to RoentGen [23] which used a training set of 35k CXR-report pairs.

To select the best generative model checkpoint we computed several metrics to measure the quality of synthetic images across three distinct axes. (a) Alignment with the provided findings text and demographics from the prompt was evaluated by using pretrained classification models trained on real images (torch XRV [29]) to predict labels for the synthetic images. (b) Similarity of generated images to real images was evaluated using Fréchet Inception Distance (FID). (c) Diversity among synthetic images generated from the same text prompt was evaluated using the image-level multi-scale structural similarity index (MS-SSIM) and the cosine similarity of BioViL [9] image embeddings. Supplementary Table 1 summarizes the synthetic image quality metrics at each model checkpoint. Based on these criteria, we selected 10k training steps (equivalent to 28 epochs) as the final RoentGen-v2 checkpoint, which required around 14 A100 GPU-hours for training. Detailed numerical data for all these criteria for checkpoint selection are provided in Supplementary Results 1.

Briefly, for our chosen checkpoint, RoentGen-v2 had an average disease area under the receiver operating characteristic curve (AUROC) of 0.81, compared to 0.88 for the real data baseline with XRV classifiers. As comparison, the original RoentGen [23] model achieved an average disease AUROC of 0.82. For demographic attributes, sex and race accuracy for synthetic images were 100% and 98%, respectively (with original XRV sex and race classifier accuracy for the real data being 97% and 95%, respectively). For the task of age prediction, we obtain comparable root mean square error (8.9 years) as the original XRV age regressor errors (7.1 years). RoentGen-v2 had an FID score of 76.8, which was considerably lower than the original RoentGen [23] model score of 96.1. Lastly, when using the same prompts for image generation, we observe a low MS-SSIM of 0.37 and moderate BioViL similarity of 0.66, indicating diversity in the generated images.

Training time for the maximum number of 60k optimization steps (equivalent to 172 epochs) was 80 A100 GPU-hours.

2.2 Synthetic Dataset

The best RoentGen-v2 checkpoint was used to generate a large and demographically balanced synthetic dataset of 565,154 samples. For each radiology report impression section in the MIMIC-CXR train set, we created multiple custom text prompts, with all possible combinations of sex (male, female) and race/ethnicity (Asian, Black, Hispanic, White) categories. For each new prompt variation, the age was randomly selected from a ± 5 year interval centered on the original age value.

We implemented a quality check step in the inference pipeline to only accept an image if the prompt matched the output of pretrained sex, race and age classifiers [29]. Each failed prompt was re-generated a maximum of three times, then discarded. We started with a total of 623,712 prompts and ended with a quality controlled dataset of 565,154 synthetic images. A total of 58,558 (9.4%) prompts failed quality check on one or more demographic attributes more than three times and were discarded. Of the 9.4% of prompts that failed to converge, 9.2% failed due to the race criterion, 0.2% due to the age criterion; none failed as a result of the sex criterion. This mode of failure is likely driven by the lack of direct imaging correlates of race as well

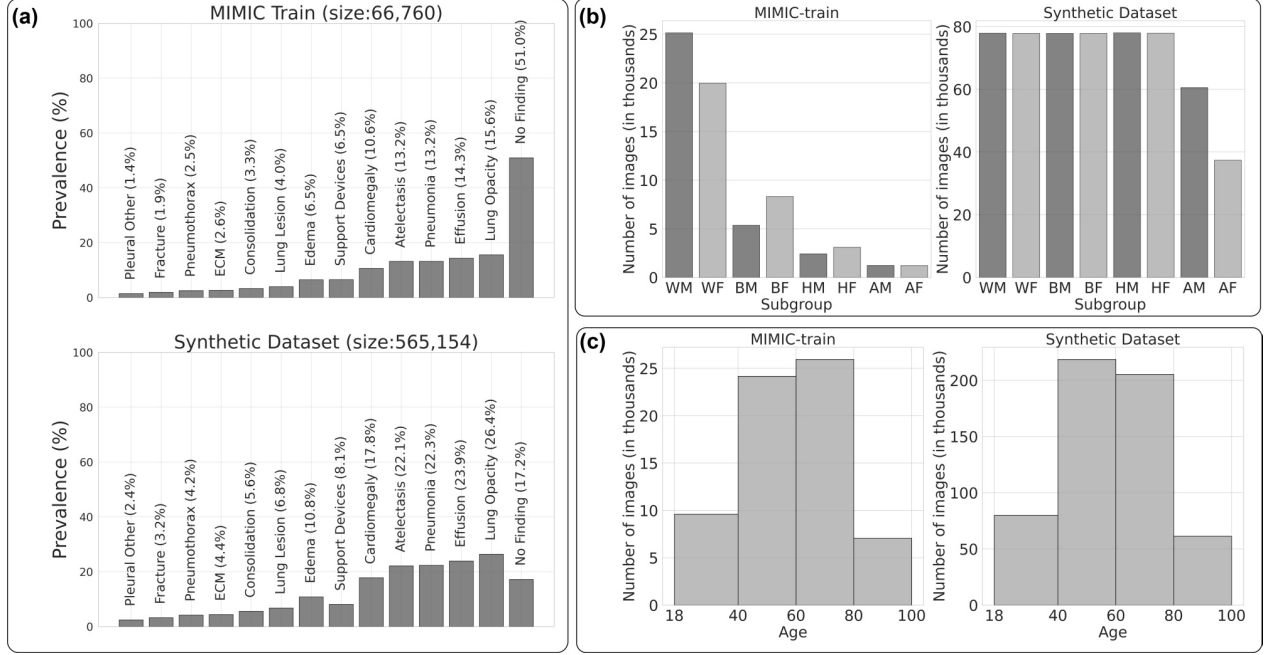


Figure 3 | Overview of label statistics for the synthetic dataset compared with the training dataset of the generative model. Panel (a) shows the prevalence for each of 13 diseases plus the ‘No Finding’ label. ECM stands for Enlarged Cardiomeastinum. Panel (b) shows the subgroup composition in terms of sex (M: male, F: female) and race/ethnicity (A: Asian, B: Black, H: Hispanic, W: White). Panel (c) shows the binned age distributions.

as pronounced class imbalance in race/ethnicity within the generative model’s training data. Among the quality-controlled synthetic images, 467,914 (83%) corresponded to text reports with one or more positive disease findings, and 97,240 (17%) displayed normal CXRs. Figure 3 shows a side-by-side comparison between the disease label distribution and demographics of the MIMIC-CXR train set and the synthetic dataset. Overall, based on our available inference compute budget and the data diversity of the training set, we successfully generated the following numbers of correctly classified synthetic CXRs: 155,728 for White demographic (3.5× increase from the original 45,102 real White CXRs), 155,653 for Black demographic (11× increase from the original 13,685 real Black CXRs), 155,870 for Hispanic demographic (28× increase from the original 5,521 real Hispanic CXRs), and 97,903 for Asian demographic (40× increase from the original 2,452 real Asian CXRs).

Total inference time, including the quality check step, was 360 A100 40GB GPU-hours for generating the final 565,154 synthetic images.

2.3 Disease Classifiers

We extend prior work to train CXR disease classifiers using synthetic data that includes disease and demographic information. Moreover, unlike prior work that naively combined synthetic and real datasets for training classifiers, we explore and identify improved mechanisms for training with synthetic data to optimize for overall classifier accuracy and fairness. We focus on out-of-distribution (OOD) evaluation using posteroanterior (PA) view CXRs from four large external datasets: CheXpert [30, 31], NIH [32], PadChest [33] and VinDr [34]. We further conduct a detailed fairness analysis by assessing intersectional subgroups of sex & race/ethnicity and sex & age across multiple datasets.

2.3.1 Synthetic Data Augmentation

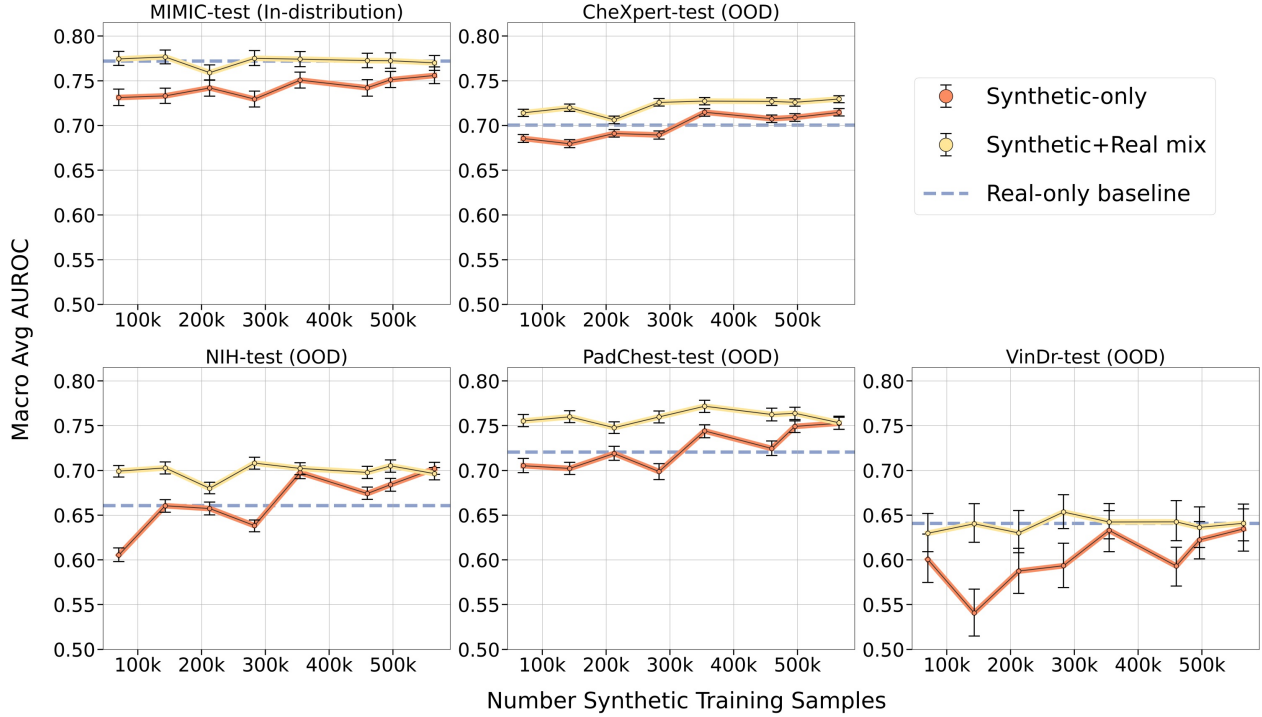


Figure 4 | Classification performance of models trained with increasing amounts of synthetic data, from the size of the real training dataset (66k samples) up to 8× the real data (565k samples). Synthetic-only models, shown in orange, are initialized from ImageNet pretrained weights and trained with varying amounts of synthetic images. Synthetic+Real mix models, shown in yellow, are initialized from ImageNet pretrained weights and trained using a combination of 66k real images plus increasing amounts of synthetic images. Blue dashed line corresponds to the baseline model, initialized from ImageNet pretrained weights and trained with 66k real images only. Y-axis shows average AUROC, error bars indicate 95% confidence intervals; X-axis shows the number of synthetic images in the train set. Each model is evaluated in-distribution on MIMIC-CXR test split and out-of-distribution (OOD) on four external datasets.

Training with a mix of real and synthetic data We trained downstream classifiers starting from ImageNet-pretrained weights and used a training set of real data from MIMIC-CXR combined with synthetic data from RoentGen-v2 (termed the synthetic+real model). We incrementally added synthetic data to the 66k real samples in the MIMIC-CXR training set, up to a maximum number of 565k synthetic images. The synthetic+real model with maximal data achieved an AUROC of 0.770 (CI: 0.762 – 0.778) for the multi-label classification task on the in-distribution MIMIC-CXR test set. This was on par with the real-only baseline which had an AUROC of 0.772 (CI: 0.765 – 0.781), and the difference between the two was not statistically significant (p-value= 0.67).

Training on synthetic+real data resulted in increased AUROC scores on out-of-distribution datasets compared to the real-only baseline: 4.3% increase on CheXpert from 0.700 (CI: 0.696 – 0.705) to 0.730 (CI: 0.725 – 0.733), 5.3% increase on NIH from 0.661 (CI: 0.654 – 0.668) to 0.696 (CI: 0.690 – 0.703), and 4.4% increase on PadChest from 0.721 (CI: 0.713 – 0.729) to 0.753 (CI: 0.746 – 0.761), all for maximal data supplementation; differences were statistically significant (p-value< 0.05). On the VinDr test set, the synthetic+real model achieved an AUROC of 0.641 (CI: 0.621 – 0.662), on par with the real-only baseline AUROC of 0.641 (CI: 0.617 – 0.663), with no significant difference between the two (p-value= 0.99). Supplementing real training data with synthetic training data improved performance on most out-of-distribution datasets. This effect plateaued at 300k synthetic samples, or about 5× the number of real data samples. Figure 4 summarizes these findings for all the intermediary data supplementation steps.

Training only with synthetic data When classifiers were trained using synthetic data alone, multi-label AUROC in-distribution remained marginally lower than that of the real-only baseline. The synthetic-only model trained on 565k images obtained an AUROC of 0.756 (CI: 0.747 – 0.766) on MIMIC-test, slightly below the real-only baseline of 0.772 (CI: 0.765 – 0.781); the difference was significant with $p\text{-value} < 0.05$. However, synthetic-only models trained with 300k or more images were able to match or surpass the performance of the real-only baseline on out-of-distribution evaluations. The synthetic-only model trained on 565k images achieved the following multi-label AUROCs on external datasets: on CheXpert, 0.715 (CI: 0.711 – 0.719) compared to real-only baseline of 0.700 (CI: 0.696 – 0.705); on NIH, 0.702 (CI: 0.696 – 0.709) compared to real-only baseline of 0.661 (CI: 0.654 – 0.668); on PadChest, 0.753 (CI: 0.746 – 0.759) compared to real-only baseline of 0.721 (CI: 0.713 – 0.729); on VinDr, 0.635 (CI: 0.610 – 0.657) compared to real-only baseline of 0.641 (CI: 0.617 – 0.663). All differences were significant with $p\text{-value} < 0.05$, except for the VinDr test set where $p\text{-value}=0.70$.

When directly comparing the synthetic-only model (trained on 565k generated images) with the synthetic+real mix model (trained on 565k generated images and 66k real images), there was no significant difference in AUROC on NIH ($p\text{-value}=0.19$), PadChest ($p\text{-value}=0.93$) and VinDr ($p\text{-value}=0.65$). On MIMIC-test, the synthetic+real model achieved slightly higher AUROC, 0.770 (CI: 0.762 – 0.778) compared to the synthetic-only model, 0.756 (CI: 0.747 – 0.766), with an associated $p\text{-value} < 0.05$. On CheXpert-test, the synthetic+real model achieved 0.730 (CI: 0.725 – 0.733), slightly higher than the synthetic-only model score of 0.715 (CI: 0.711 – 0.719), with a corresponding $p\text{-value} < 0.05$. When using fewer generated images in the train set, differences between the synthetic+real and synthetic-only models were more pronounced, as illustrated in Figure 4. Overall, we unsurprisingly find that training on synthetic data can always benefit from the addition of real data.

2.3.2 Synthetic pretraining

It is common practice in the computer vision literature to initialize models with weights pretrained on natural image datasets such as ImageNet. We propose an analogous supervised pretraining strategy that performs pretraining with synthetic CXR data instead of natural images, followed by supervised fine-tuning on MIMIC-CXR train set (real data only). Figure 5 illustrates the benefits of synthetic pretraining when fine-tuning classifiers on varying amounts of real data. Synthetic pretraining led to consistent AUROC improvements over the real-only baseline (initialized from ImageNet weights) both in- and out-of-distribution. When fine-tuning the synthetic-pretrained model using the maximum available real data (66k images), we observed the following performance gains: on MIMIC-CXR a 3.3% increase from 0.772 (CI: 0.765 – 0.781) to 0.798 (CI: 0.791 – 0.806), on CheXpert a 4.5% increase from 0.700 (CI: 0.696 – 0.705) to 0.732 (CI: 0.728 – 0.736), on NIH a 9.8% increase from 0.661 (CI: 0.654 – 0.668) to 0.726 (CI: 0.720 – 0.733), on PadChest a 8.3% increase from 0.721 (CI: 0.713 – 0.729) to 0.781 (CI: 0.773 – 0.789), and on VinDr a 6.5% increase from 0.641 (CI: 0.617 – 0.663) to 0.683 (CI: 0.662 – 0.704). All differences were statistically significant with $p\text{-value} < 0.05$.

Moreover, when using synthetic pretraining, by fine-tuning on less than 10k real samples, we match or exceed the AUROC of the real-only baseline trained on the full 66k real samples (illustrated by the dashed blue line in Figure 5). Also, when using synthetic pretraining and fine-tuning on 30k or more real samples, we exceed the AUROC of the synthetic+real mix model trained on the combination of all available data (illustrated by the dashed yellow line in Figure 5). This improvement was statistically significant ($p\text{-value} < 0.05$) on MIMIC, NIH, PadChest, and VinDr, but not on CheXpert test dataset. Overall, pretraining with synthetic data can improve performance over ImageNet pretraining or can achieve the same performance with dramatic reductions in the need for real training data. Furthermore, two-stage training that combines supervised pretraining with synthetic data followed by fine-tuning with real data outperforms naively mixing synthetic and real data together, as is the norm in prior studies.

Figure 6 shows the overall AUROC comparison between the best performing models from each training strategy, using the maximally available training data: (i) Real-only baseline model (trained on 66k real CXRs), (ii) Synthetic-only model (trained on 565k synthetic CXRs), (iii) Synthetic+Real mix model (trained on combined 66k real CXRs and 565k synthetic CXRs), and (iv) Synthetic-pretrained model (supervised pretraining on 565k synthetic CXRs, followed by fine-tuning on 66k real-only CXRs). In scenarios (i)–(iii) models were initialized using ImageNet pretrained weights; in scenario (iv) the model was trained from scratch.

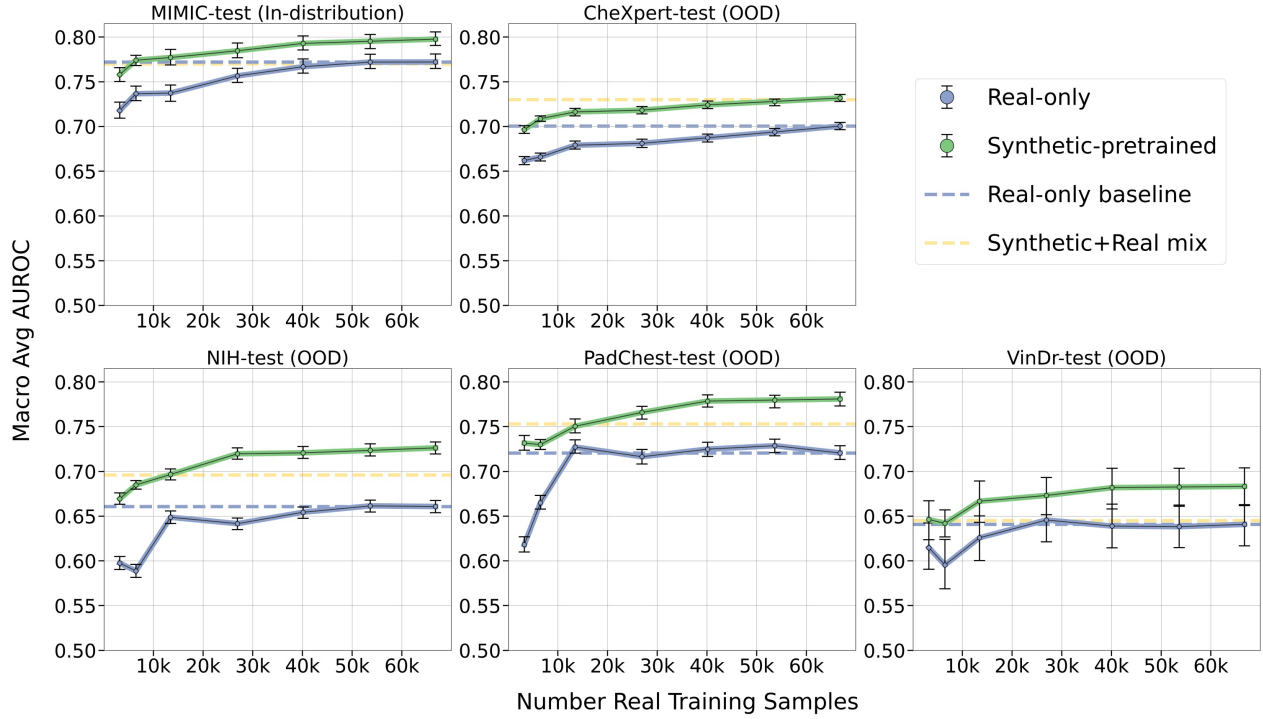


Figure 5 | Classification performance of models trained with varying amounts of real data, from the maximally available 66k samples down to data-scarce regimes with as little as 3k samples. Real-only models, shown in blue, are initialized from ImageNet pretrained weights and trained with varying amounts of real images. The blue dashed line corresponds to the baseline model trained with all 66k real images. Synthetic-pretrained models, shown in green, are first pretrained from scratch with 565k synthetic images, then fine-tuned with increasing amounts of real images. Yellow dashed line corresponds to the Synthetic+Real mix model, initialized from ImageNet pretrained weights and trained with all available data (66k real images and 565k synthetic images). Y-axis shows average AUROC, error bars indicate 95% confidence intervals; x-axis shows the number of real images in the train set. Each model is evaluated in-distribution on MIMIC-test and out-of-distribution (OOD) on four external datasets.

The synthetic pretraining strategy yielded the best multi-label AUROC performance across all datasets. In-distribution, on MIMIC-test, the synthetic-pretrained model achieved an AUROC of 0.798 (CI: 0.791 – 0.806), above the real-only baseline of 0.772 (CI: 0.765 – 0.781) and the synthetic+real mix model of 0.770 (CI: 0.762 – 0.778). Out-of-distribution, on CheXpert-test, the synthetic-pretrained model achieved an AUROC of 0.732 (CI: 0.728 – 0.736), on par with the synthetic+real mix model of 0.730 (CI: 0.725 – 0.733), both above the real-only baseline of 0.700 (CI: 0.696 – 0.705). On NIH-test, the synthetic-pretrained model achieved an AUROC of 0.726, (CI: 0.720 – 0.733), above the synthetic+real mix model of 0.696 (CI: 0.690 – 0.703), and the real-only baseline of 0.661 (CI: 0.654 – 0.668). On PadChest-test, the synthetic-pretrained model achieved an AUROC of 0.781 (CI: 0.773 – 0.789), above the synthetic+real mix model of 0.753 (CI: 0.746 – 0.761), and the real-only baseline of 0.721 (CI: 0.713 – 0.729). Finally, on VinDr-test, the synthetic-pretrained model achieved an AUROC of 0.683 (CI: 0.662 – 0.704), above the real-only baseline of 0.641 (CI: 0.617 – 0.663) and the synthetic+real mix model of 0.641 (CI: 0.621 – 0.662). All pairwise AUROC differences between the synthetic-pretrained model and other models were statistically significant with $p\text{-value} < 0.05$ under the DeLong test unless specified otherwise. Supplementary Figure 11 shows disease-specific AUROC metrics across all models and datasets (discussed in Supplementary Note 1).

The synthetic pretraining strategy also yielded the highest multi-label area under the precision recall curve (AUPRC) values. In-distribution, on MIMIC-test, the synthetic-pretrained model achieved an AUPRC of 0.360 (CI: 0.350 – 0.374), above the synthetic+real mix model of 0.331 (CI: 0.322 – 0.344) and the real-only baseline of 0.316 (CI: 0.307 – 0.329). Out-of-distribution, on CheXpert-test, the synthetic-pretrained model achieved an AUPRC of 0.324 (CI: 0.320 – 0.330), on par with the synthetic+real mix model of 0.323 (CI: 0.318 – 0.329), both above the real-only baseline of 0.284 (CI: 0.280 – 0.289). On NIH-test, the synthetic-pretrained model achieved

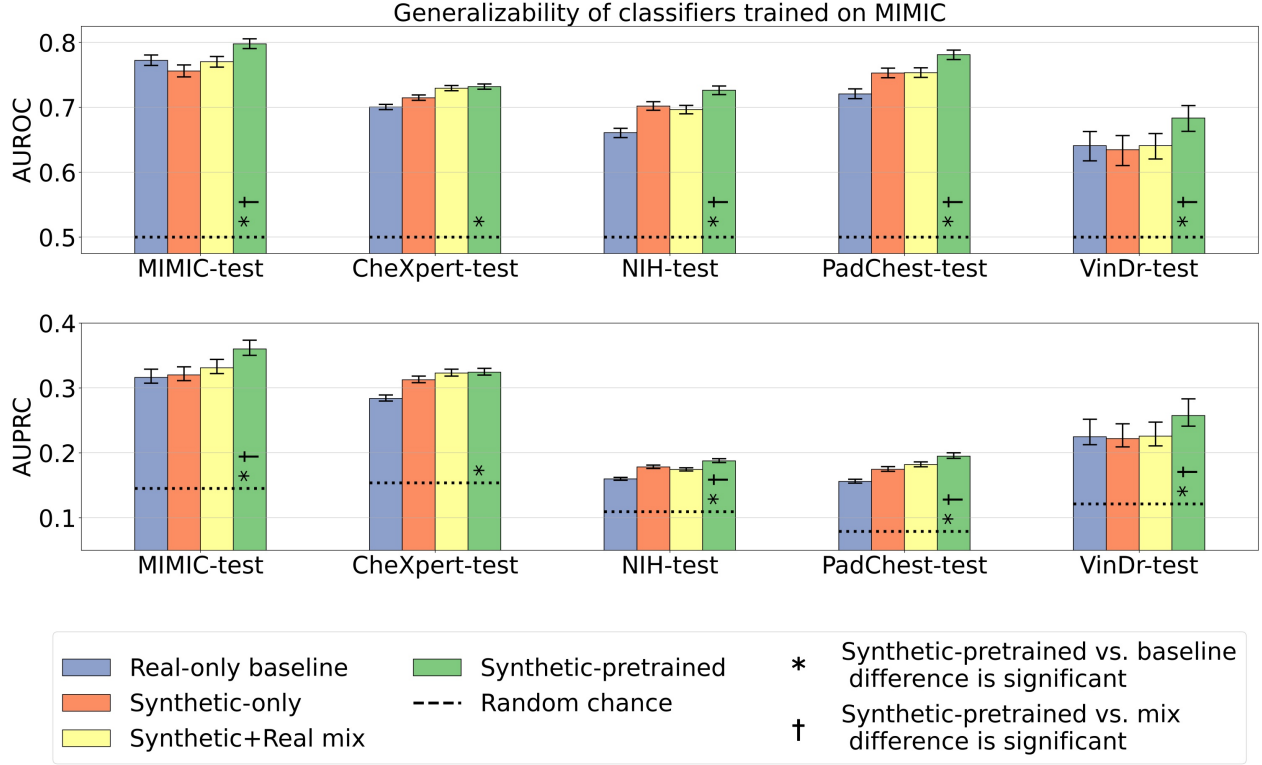


Figure 6 | Classification performance of models trained on all available real and/or synthetic data according to four strategies: (i) Real-only (baseline) model trained on 66k real CXRs, (ii) Synthetic-only model trained on 565k synthetic CXRs, (iii) Synthetic+Real mix model trained on combined 66k real and 565k synthetic CXRs, and (iv) Synthetic-pretrained model, which underwent supervised pretraining on 565k synthetic CXRs followed by fine-tuning on 66k real CXRs. In scenarios (i)–(iii) models were initialized using ImageNet pretrained weights; in scenario (iv) the model was trained from scratch. Y-axis shows macro-average multi-label AUROC (top panel), and AUPRC (bottom panel), with error bars indicating 95% confidence intervals. Each model is evaluated in-distribution on MIMIC-test and out-of-distribution on four external datasets.

an AUPRC of 0.188, (CI: 0.185 – 0.191), above the synthetic+real mix model of 0.174 (CI: 0.172 – 0.177), and the real-only baseline of 0.160 (CI: 0.158 – 0.162). On PadChest-test, the synthetic-pretrained model achieved an AUPRC of 0.195 (CI: 0.191 – 0.200), above the synthetic+real mix model of 0.182 (CI: 0.179 – 0.186), and the real-only baseline of 0.156 (CI: 0.153 – 0.159). Finally, on VinDr-test, the synthetic-pretrained model achieved an AUPRC of 0.258 (CI: 0.241 – 0.283), above the real-only baseline of 0.225 (CI: 0.212 – 0.252) and the synthetic+real mix model of 0.226 (CI: 0.211 – 0.247). All pairwise AUPRC differences between the synthetic-pretrained model and other models were statistically significant with $p\text{-value} < 0.05$ under the permutation test unless specified otherwise. Supplementary Figure 12 shows disease-specific AUPRC metrics across all models and datasets (discussed in Supplementary Note 1).

2.3.3 Classifier Fairness

Beyond boosting classifier performance and generalization with synthetic data, we also investigate how synthetic data impacts classifier fairness. We measure fairness using the following metrics: (a) subgroup-level classification performance (multi-label AUROC), (b) average performance gap between the best and worst performing subgroups as per [27], and (c) underdiagnosis gap between the best and worst performing subgroups as proposed by [18, 20]. We analyzed intersectional subgroups, here defined as patients who belong to two subpopulations (e.g. a female patient of Hispanic ethnicity). This is motivated by prior work showing that intersectional subgroups often have compounded algorithmic biases [18]. Based on the availability of metadata, we define subgroups both by intersection of sex & race/ethnicity (e.g. Black female) and sex & age (e.g. male aged 40-60 years old) for MIMIC-CXR and CheXpert. We define subgroups by intersection of sex & age

attributes for NIH and PadChest datasets. Since either sex and/or age data are missing for over 83% of patients in VinDr-test, we do not perform subgroup analysis for this dataset.

(a) Subgroup Classification Performance For each model, we calculated the macro-average multi-label AUROC for all intersectional subgroups. In Figure 7, we depict the AUROCs of each subgroup for the best model in each training paradigm. We observe that synthetic pretraining reliably improves classification performance in all demographic subgroups across all datasets. For subgroups defined by sex & race/ethnicity, the synthetic-pretrained model boosted performance over baseline in 7 out of 8 subgroups on MIMIC (there was no significant difference from baseline for the Asian female subgroup), and in all 8 out of 8 subgroups on CheXpert. For subgroups defined by sex & age, the synthetic-pretrained model boosted performance over baseline in all 8 out of 8 subgroups on MIMIC, CheXpert, NIH and PadChest. Therefore, the proposed synthetic pretraining method maximally reduces fairness gaps by providing performance benefits irrespective of protected demographic attributes.

(b) Average Performance Gap For each model, we calculated the average AUROC in all intersectional subgroups. We define the *fairness gap* as the difference between the best and worst performing subgroups. Similar to [27], we plot the fairness gap against average AUROC for all trained models, evaluated in-distribution and on out-of-distribution test sets (Figure 8). On average, for in-distribution evaluation on MIMIC, we observed little to no difference in the fairness gap between the baseline and synthetic-pretrained model, while multi-label AUROC improved by 3.3%. Out-of-distribution synthetic pretraining led to smaller fairness gaps by 16.0% on average, while improving multi-label AUROC by an average 7.3%.

For sex & race/ethnicity subgroups, on MIMIC, the baseline fairness gap was 0.149 (CI: 0.110 – 0.188) and the synthetic-pretrained fairness gap was 0.149 (CI: 0.105 – 0.193). On CheXpert, the baseline fairness gap was 0.051 (CI: 0.027 – 0.075) and the synthetic-pretrained fairness gap was 0.038 (CI: 0.021 – 0.055), a 25.5% reduction.

For sex & age subgroups, the synthetic-pretrained model achieved the smallest fairness gap on 3 out of 4 evaluation datasets. On MIMIC, the baseline fairness gap was 0.110 (CI: 0.084 – 0.137) and the synthetic-pretrained fairness gap was 0.104 (CI: 0.084 – 0.123), a 5.5% reduction. On CheXpert, the baseline fairness gap was 0.114 (CI: 0.096 – 0.133) and the synthetic-pretrained fairness gap was 0.085 (CI: 0.074 – 0.097), a 25.4% reduction. On NIH, the baseline fairness gap was 0.210 (CI: 0.164 – 0.256) and the synthetic-pretrained fairness gap was 0.168 (CI: 0.153 – 0.184), a 20.0% reduction. Finally, on PadChest, the baseline fairness gap was 0.295 (CI: 0.259 – 0.331) and the synthetic-pretrained fairness gap was 0.315 (CI: 0.287 – 0.342), a 6.8% increase.

(c) Underdiagnosis Gap Multiple studies consider underdiagnosis as a primary criteria for fairness, due to its potentially harmful impact on patient outcomes, such as not receiving a treatment or receiving one with a delay. Following [18, 20], we define the *underdiagnosis rate* as the false-positive rate (FPR) of the binarized model prediction for the ‘No Finding’ label, indicating a missed diagnosis. We compute this underdiagnosis rate at the levels of intersectional subgroups. The corresponding *underdiagnosis gap* is the difference between subgroups with the highest and lowest FPRs for each model. Figure 9 plots the underdiagnosis gap against average model AUROC for the best model in each training paradigm. The use of synthetic data, either as augmentation strategy or pretraining strategy reduced the underdiagnosis gap across all datasets compared to the real-only baseline. On average across datasets, synthetic pretraining led to a 19.3% decrease in the underdiagnosis gap, while increasing multi-label AUROC by 6.5%.

For sex & race/ethnicity subgroups on MIMIC, the baseline underdiagnosis gap was 0.260 (CI: 0.213 – 0.307) and the synthetic-pretrained underdiagnosis gap was 0.210 (CI: 0.180 – 0.241), a 19.2% reduction. On CheXpert, the baseline underdiagnosis gap was 0.123 (CI: 0.096 – 0.150) and the synthetic-pretrained underdiagnosis gap was 0.099 (CI: 0.076 – 0.122), a 19.5% reduction.

For sex & age subgroups, the synthetic-pretrained model achieved smaller underdiagnosis gaps on 4 out of 4 evaluation datasets. The smallest underdiagnosis gaps were displayed by the synthetic-only models, followed by the synthetic+real mix models. On MIMIC, the baseline underdiagnosis gap was 0.614 (CI: 0.560 – 0.667) and the synthetic-pretrained underdiagnosis gap was 0.519 (CI: 0.459 – 0.579), a 15.5% reduction. On CheXpert, the baseline underdiagnosis gap was 0.434 (CI: 0.415 – 0.453) and the synthetic-pretrained

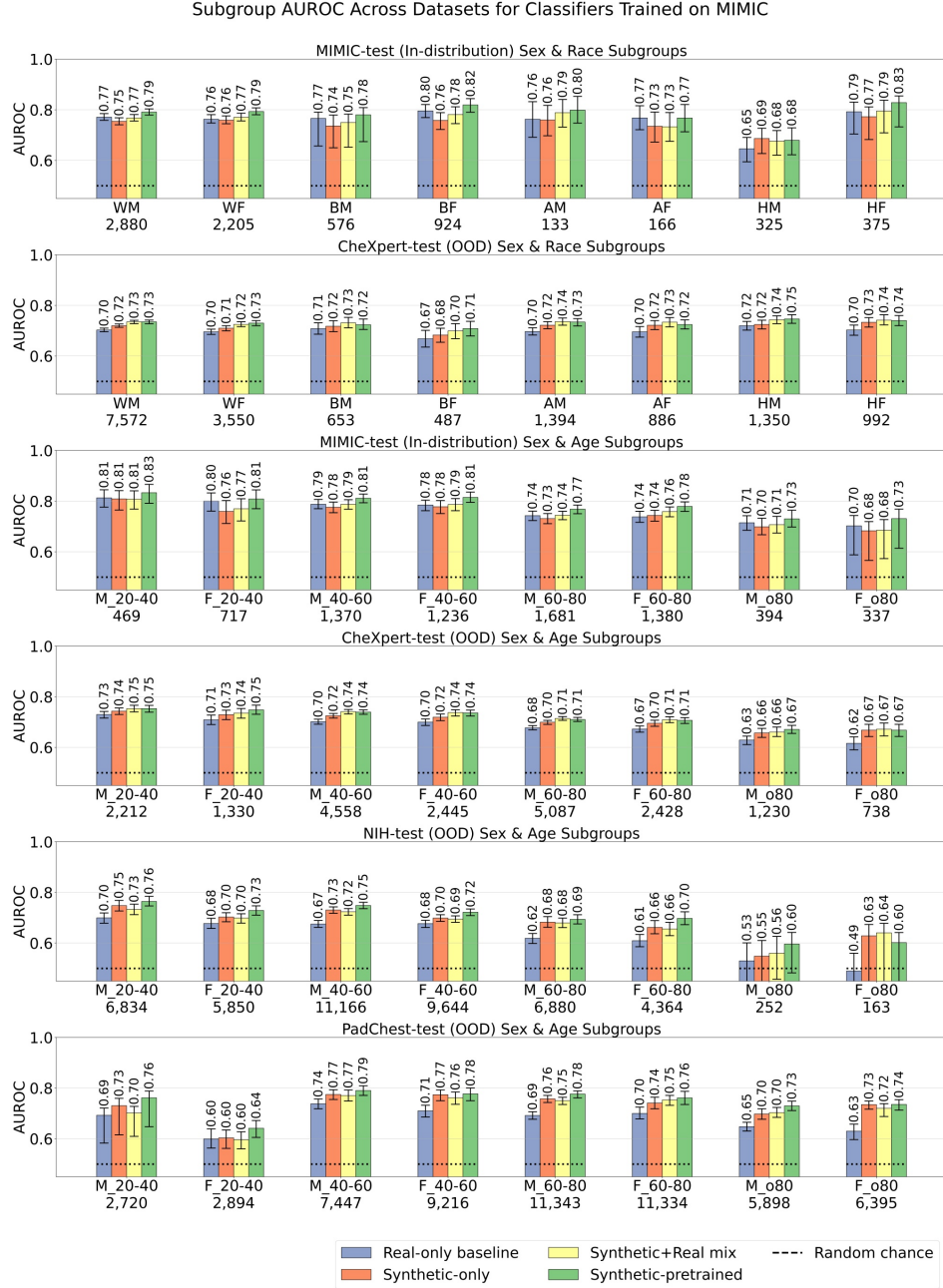


Figure 7 | Subgroup classification performance of models trained on all available real and/or synthetic data according to four strategies: (i) Real-only (baseline) model trained on 66k real CXRs, (ii) Synthetic-only model trained on 565k synthetic CXRs, (iii) Synthetic+Real mix model trained on combined 66k real and 565k synthetic CXRs, and (iv) Synthetic-pretrained model, which underwent supervised pretraining on 565k synthetic CXRs followed by fine-tuning on 66k real CXRs. In scenarios (i)–(iii) models were initialized using ImageNet pretrained weights; in scenario (iv) the model was trained from scratch. Y-axis shows macro-average multi-label AUROC, with each panel focusing on one dataset. MIMIC-test is in-distribution, while CheXpert, NIH, and PadChest are out-of-distribution. A random chance classifier would score 0.50 AUROC. Top two rows use subgroups defined by sex & race/ethnicity (M: male, F: female, W: White, B: Black, H: Hispanic, A: Asian). Remaining rows use subgroups defined by sex & age. On the x-axis, below each subgroup’s label is the patient count of the subgroup.

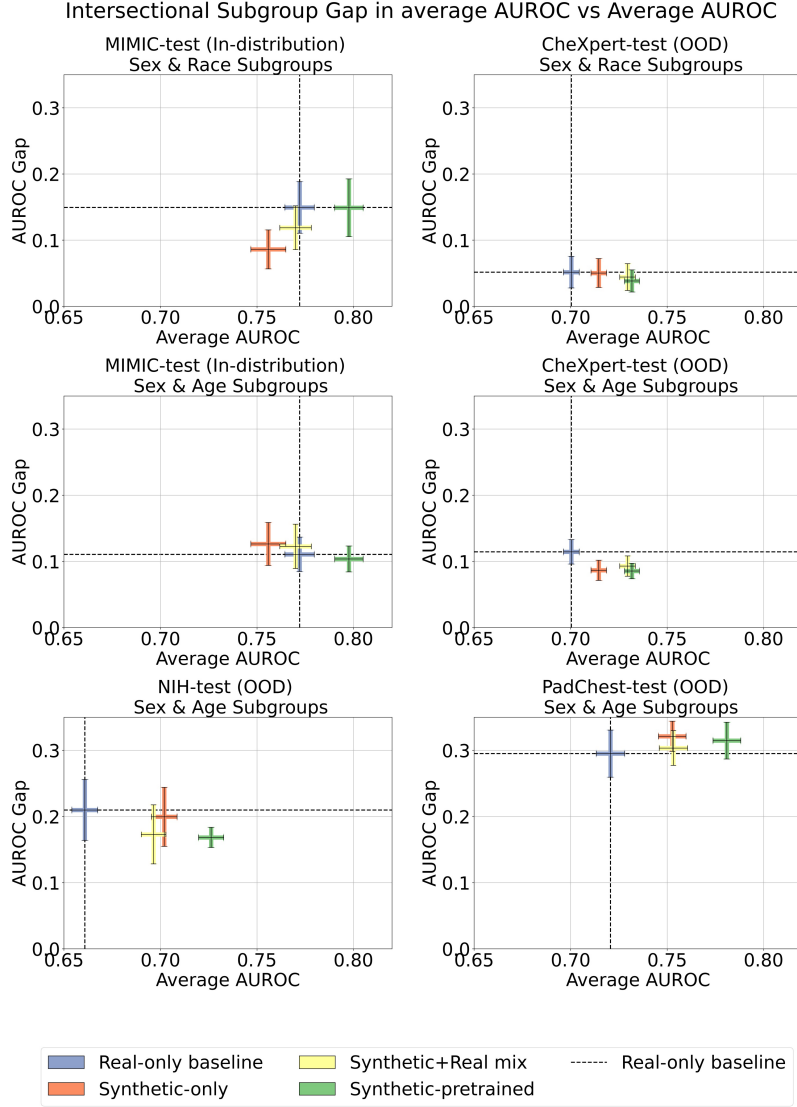


Figure 8 | Fairness gap in classifier AUROC across intersectional subgroups. Top row uses subgroups defined by sex & race/ethnicity, middle and bottom rows use subgroups defined by sex & age. Y-axis measures fairness gap between the best and worst performing subgroup for each model; lower values indicate better fairness. X-axis measures average model AUROC in the entire test population; higher values indicate better overall classification performance. Models were trained on all available real and/or synthetic data according to four strategies: (i) Real-only (baseline) model trained on 66k real CXRs, (ii) Synthetic-only model trained on 565k synthetic CXRs, (iii) Synthetic+Real mix model trained on combined 66k real and 565k synthetic CXRs, and (iv) Synthetic-pretrained model, which underwent supervised pretraining on 565k synthetic CXRs followed by fine-tuning on 66k real CXRs. In scenarios (i)–(iii) models were initialized using ImageNet pretrained weights; in scenario (iv) the model was trained from scratch.

underdiagnosis gap was 0.346 (CI: 0.325 – 0.367), a 20.3% reduction. On NIH, the baseline underdiagnosis gap was 0.349 (CI: 0.275 – 0.422) and the synthetic-pretrained underdiagnosis gap was 0.269 (CI: 0.213 – 0.325), a 22.9% reduction. On PadChest, the baseline underdiagnosis gap was 0.603 (CI: 0.580 – 0.626) and the synthetic-pretrained underdiagnosis gap was 0.490 (CI: 0.460 – 0.521), a 18.7% reduction.

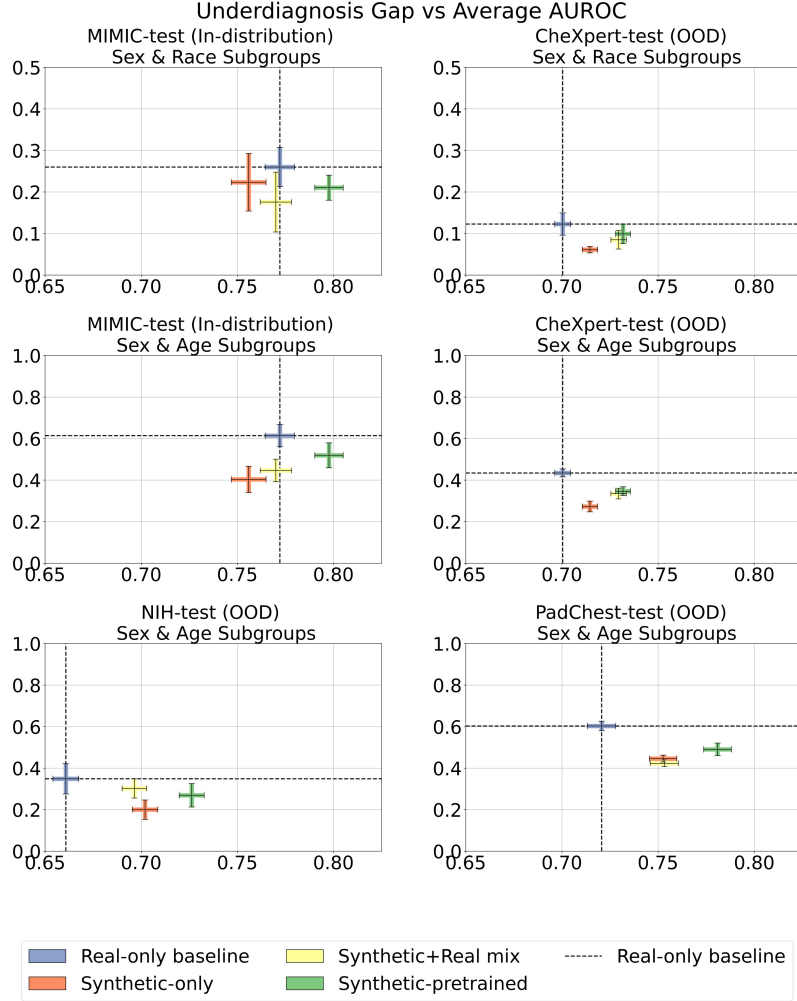


Figure 9 | Underdiagnosis gap in classifiers across intersectional subgroups. Top row uses subgroups defined by sex & race/ethnicity, middle and bottom rows use subgroups defined by sex & age. Y-axis measures underdiagnosis (False Positive Rate of ‘No Finding’ label) gap between the best and worst performing subgroup for each model; lower values indicate better fairness. X-axis measures average model AUROC in the entire test population; higher values indicate better overall classification performance. Models were trained on all available real and/or synthetic data according to four strategies: (i) Real-only (baseline) model trained on 66k real CXRs, (ii) Synthetic-only model trained on 565k synthetic CXRs, (iii) Synthetic+Real mix model trained on combined 66k real and 565k synthetic CXRs, and (iv) Synthetic-pretrained model, which underwent supervised pretraining on 565k synthetic CXRs followed by fine-tuning on 66k real CXRs. In scenarios (i)–(iii) models were initialized using ImageNet pretrained weights; in scenario (iv) the model was trained from scratch.

3 Discussion

Our study conducted a detailed investigation into how classifier performance and fairness generalize when leveraging a large, demographically balanced synthetic dataset. Specifically, we demonstrated that text-conditioned latent diffusion models can generate synthetic chest radiographs with fine-grained control over both radiographic findings and key demographic attributes, including sex, age and race/ethnicity. To ensure fidelity, we incorporated rigorous quality control measures into the inference pipeline, filtering out low-quality or misaligned samples to retain only those that accurately matched the conditioning prompts.

We trained downstream classifiers using four distinct strategies: (i) Using only real CXRs; (ii) Using only synthetic CXRs generated by RoentGen-v2 ; (iii) Augmenting real CXRs with synthetic CXRs as is common in the literature; (iv) A two-stage data-centric training, where we first perform supervised pretraining with

synthetic CXRs, followed by fine-tuning on real CXRs. In scenarios (i)–(iii) models were initialized using ImageNet pretrained weights; in scenario (iv) models were pretrained from scratch using the synthetic data, then fine-tuned on real-only data.

Prior works have trained disease classifiers using a mix of real and synthetic data. Khosravi et al. [26] reported a 2.8% increase in multi-label AUROC over baseline when using $10\times$ unconditional synthetic data supplementation; training with purely synthetic data ($2\times$ the number of real samples) matched the performance of the real-only baseline, but remained below that of the model trained with real and synthetic data. Ktena et al. [27] reported a 5.2% increase in multi-label AUROC over the real-only baseline when training a model on synthetic images only. Our first set of experiments verified that supplementing real datasets with synthetic data enhances model performance and generalization, and that synthetic data alone does not match the mixed models. On average across five evaluation datasets, the model trained only on synthetic images increased AUROC by 2.1% over the real-only baseline, while the model trained on real and synthetic images increased AUROC by 2.7%. Next, we enhanced current best practices by showing that synthetic images used during pretraining instead of as a data augmentation step further boosts classification performance across all datasets, leading to an average 6.5% increase in AUROC. Our proposed pretraining strategy also increased robustness when fewer real samples were available for fine-tuning. By fine-tuning on less than $10k$ real samples, the synthetic-pretrained models matched or exceeded the AUROC of the real-only baseline trained on the full $66k$ real samples ($6\times$ more). When fine-tuning on $30k$ or more real samples, the synthetic-pretrained models exceeded the AUROC of the synthetic+real mix model trained on the combination of all available data. None of the prior works investigated this low-data regime.

Next, motivated by prior work showing that intersectional subgroups often have compounded algorithmic biases [18], we conducted a detailed fairness analysis on intersectional subgroups of sex & age and sex & race/ethnicity. Prior literature has assessed fairness of CXR classifiers using a variety of different metrics, where each metric has a different calculation and interpretation of fairness [17, 20, 27]. Only one study [27] probed the impact of synthetic data on fairness, and the analysis was limited to one metric (fairness gap) for subgroups defined by a single protected attribute (sex or race), on one out-of-distribution dataset. In our experiments, for intersectional subgroups across four datasets, synthetic pretraining led to an average 16.0% decrease in the fairness gap, and a 19.3% decrease in the underdiagnosis gap. Notably, average classification performance measured by AUROC increased across subgroups, irrespective of protected attributes. Independent of the fairness metrics used, we showed that our synthetic data generation pipeline and data-centric synthetic pretraining approach enhance fairness in a generalized manner across several out-of-distribution datasets.

Our results should be interpreted with attention to some limitations. First, we trained RoentGen-v2 on one source dataset (MIMIC-CXR), and used only one radiographic view (PA), which limits the expressive power of the generative model. The effects could be observed at inference time, where for example the model was not able to produce as many correct samples of Asian patients, likely owing to the much smaller training sample size for that population. Second, when generating the synthetic dataset, we replicated the training dataset label distribution without changing disease prevalence. In future studies, oversampling of specific diseases with the low prevalence should be investigated for long-tailed disease classification. Third, all classifiers are trained on datasets where disease labels were automatically extracted from radiology reports using the Chexpert labeler [35]. Since this tool relies on rule-based natural language processing techniques, some of these labels may be incorrect, in ways that could compound with observed biases or model errors. Lastly, while synthetic data holds great promise for advancing model development in healthcare, further research is needed to ensure privacy preservation and prevent patient re-identification that may occur through data memorization [36].

Overall, our results demonstrate that high-quality, text and demographically controllable synthetic data can serve as a powerful complement to real datasets, improving both performance and fairness in medical imaging deep learning, especially when real data are imbalanced, scarce, or difficult to obtain.

4 Methods

4.1 RoentGen-v2 Training

Dataset Our aim was to train a high-quality text-to-image diffusion model where the text prompt is derived from the radiology report impression section as well as patient demographics (sex, age, race/ethnicity). We curated a paired image-text-demographics triplet dataset from the publicly available MIMIC-CXR [28] data (version 2.0.0). MIMIC-CXR consists of 377k CXRs and corresponding text reports obtained from 228k patients at the Beth Israel Deaconess Medical Center (Boston, MA, United States). We started with all available 377,095 images from MIMIC-CXR. Our exclusion criteria included radiographic views other than postero-anterior, missing or non-descriptive impression section in the radiology report, missing sex or age information, and race/ethnicity not belonging to the Asian, Black, Hispanic, White categories. Following our exclusions, our dataset consisted of a total 75,639 studies from MIMIC-CXR, with triplets of images, radiology reports, and demographic metadata (CONSORT diagram in Supplementary Figure 10). MIMIC-CXR is organized into ten folders (p10-p19). Based on prior studies [23], images belonging to p19 folder were used as a held-out test split (7,584 images). The images belonging to folders p10-p18 were divided into training (66,760 images) and validation (1,295 images) splits. No patients were shared across training, validation, and testing splits. Supplementary Table 2 presents more details regarding the data composition of each split. For each triplet of images, radiology reports, and demographic information we constructed a text prompt with the following structure: <AGE> year old <RACE> <SEX>. <IMPRESSION>. If the resulting prompt exceeded the 77 token limit of the CLIP text encoder [37], we abbreviated the impression using GPT-4 [38], based on prior work demonstrating that GPT-4 is highly capable in summarizing radiology reports [39, 40]. For this summarization task, the GPT-4 prompt was: “Your task is to summarize this radiology report within 200 characters or less. Your response must be concise, truthful, and keep all relevant medical information.”. A total of 6,072 impressions were summarized in this manner.

Training The training procedure for RoentGen-v2 followed best practices established in the original RoentGen paper [23]. We used Stable Diffusion [41](version 2.1) as the underlying model with CLIP ViT-L/14 text encoder (77 token limit). This was a newer version compared to the original RoentGen [23] built upon Stable Diffusion version 1.4. We jointly fine-tuned the text encoder and U-Net with learning rate 5×10^{-5} for up to 60k optimization steps. We used AdamW optimizer and constant learning rate scheduler with 500 warmup steps. Training was performed on four A100 GPUs with 40GB vRAM each, allowing a batch size of 192.

4.2 RoentGen-v2 Evaluation and Checkpoint Selection

For each model checkpoint, inference was performed using text prompts from the MIMIC-CXR validation set. Four synthetic images were generated per prompt using different random seeds to capture variability. Each synthetic image was paired with its corresponding real image, disease labels, and demographic attributes from the validation set. These pairs were used to compute a range of quality metrics, which guided the selection of the optimal model checkpoint for downstream experiments.

Text Prompt Alignment To evaluate how accurately RoentGen-v2 adhered to the provided text prompts, we used pretrained classifiers from the Torch X-ray Vision (XRV) library [29]. For disease classification, we used the XRV DenseNet-121 model to compute the Area Under the Receiver Operating Characteristic curve (AUROC) for detecting Atelectasis, Cardiomegaly, Edema, Pneumothorax, and Pleural Effusion. For sex classification, we used the sex prediction model from [42] and assessed performance using accuracy. For race classification, we used the XRV race model and evaluated accuracy. For age prediction, we used the XRV age model, reporting performance as the root mean square error (RMSE) in years. Since the images generated by RoentGen-v2 were at a resolution of 512×512 pixels (higher than the 224×224 pixel input size expected by the XRV models) we downsampled the synthetic images using area-based interpolation prior to inference.

Real-Synthetic Image Similarity Assessment We evaluated the similarity between real and synthetic images by comparing both the raw images and their embeddings extracted from natural and biomedical image encoders, as detailed below. The Fréchet Inception Distance (FID) score [43] quantifies the difference between the distributions of generated images and real ground truth images. Specifically, FID calculates the mean

and covariance of embeddings derived from the deepest layer of the Inception v3 network [44], effectively measuring the similarity of high-level feature representations across the two image sets. A higher FID score indicates poorer generative performance, whereas a score of zero reflects a perfect match.

Recognizing that the conventional FID embeddings come from a network pretrained on natural images, we additionally generated embeddings using a model trained specifically on medical images. We used the encoder from the BioViL [9], a state-of-the-art CXR interpretation model to compute cosine similarity between embeddings of real images and their corresponding synthetic images generated from the same prompts. A cosine similarity score of 1 denotes identical embeddings, implying high fidelity in the synthetic images.

Furthermore, we calculated the multi-scale structural similarity index (MS-SSIM) between the distributions of real and synthetic images. MS-SSIM values range from 0 to 1, where 1 indicates identical images and 0 signifies no similarity. Importantly, neither extreme is desirable in this context, as MS-SSIM of 1 would reflect overfitting to the training data. Similarly, MS-SSIM of 0 would imply no similarity between generated images and their real counterparts, reflecting a severe degradation in the synthetic images’ fidelity to typical CXRs. We considered similarity scores below 0.25 as indicative of failure to produce realistic CXRs.

Intra-Prompt Image Diversity For each text prompt in the validation set, four distinct synthetic images were generated with different random seeds. To quantify visual similarity among images produced from the same prompt, we computed average pairwise MS-SSIM for all four images. This per-prompt MS-SSIM reflects intra-prompt synthetic image similarity, with a value of 1 indicating identical images and lower values indicating greater variability. The per-prompt MS-SSIM scores were then averaged across all prompts in the validation set, and the final mean MS-SSIM score reported as an overall measure of image-level intra-prompt diversity of the synthetic dataset.

Beyond image similarity, we also computed embedding similarity by measuring pairwise cosine distance between the BioViL embeddings of the four synthetic images generated per prompt. A score of 1 indicates that the images are embedding-wise identical, while lower values reflect greater variability in semantic content as captured by the BioViL model. These per-prompt cosine similarity scores were then averaged across all prompts in the validation set, and the final mean BioViL score reported as an overall measure of embedding-level intra-prompt diversity of the synthetic dataset.

For both mean MS-SSIM and mean BioViL, a score of 1 indicates that all generated images are identical (model collapse), and lower scores indicate higher variability, which is desirable in the context of generative diversity.

4.3 Synthetic Dataset Generation

To generate a demographically balanced synthetic dataset, we constructed customized text prompts as follows. For each impression in the MIMIC-CXR training split, we created all possible combinations of sex (male, female) and race/ethnicity (White, Black, Asian, Hispanic), resulting in eight demographic variations per impression. For each variation, we randomly sampled an age within ± 5 years of the original patient age. These demographic attributes were prepended to the original impression text to form the final prompt. Image generation was performed using classifier-free guidance with a scale of 4.0 and the default noise scheduler, running inference for 75 steps to produce one image per prompt. To ensure high fidelity to the specified demographic attributes and overall image quality, we implemented a quality control (QC) pipeline as follows. Each batch of generated images was evaluated using three pretrained XRV classifiers: one for sex, one for race, and one for age prediction. A synthetic image only passed quality control if the predicted sex and race exactly matched the specified value in the prompt and if the predicted age was within ± 7 years of the age specified in the prompt. The value of ± 7 years was chosen equal to the measured standard deviation of the XRV age regression model when applied to real data. Images that failed any of these criteria were discarded. All failed prompts were logged along with their failure mode, and a new round of image generation and QC was conducted on these prompts. Due to compute constraints, each failed prompt was re-generated a maximum of three times, then fully discarded. Only high-quality images that passed our rigorous QC were retained for downstream analysis.

4.4 Downstream Disease Classifier Training

Datasets The same MIMIC-CXR splits described above were used for the train, validation, and distribution testing of disease classifiers. For out-of-distribution evaluation, we used four external chest radiography datasets: CheXpert [30, 31], NIH [32], PadChest [33] and VinDr [34]. CheXpert dataset consists of 224k CXRs from 65k patients at Stanford Health Care Hospital (Stanford, CA, United States). NIH ChestX-ray dataset consists of 112k CXRs from 30k patients at the National Institutes of Health Clinical Center (Bethesda, MD, United States). PadChest dataset consists of 160k CXRs from 67k patients at San Juan Hospital (Alicante, Spain). VinDr-CXR dataset consists of 18k CXRs collected from the Hospital 108 and the Hanoi Medical University Hospital, two of the largest hospitals in Vietnam. We included posteroanterior (PA) views only; in the case of VinDr, all images are frontal views but not specified whether PA or AP. For subgroup analysis, we used sex, age and race/ethnicity information available in MIMIC-CXR and CheXpert. We used sex and age information available in NIH and PadChest. We did not perform subgroup analysis on VinDr, since only a small number of patients had demographic information available. Supplementary Table 2 summarizes the statistics of all image datasets.

Downstream Classifier Training We trained a 121-layer DenseNet models for multi-label classification task on the 14 CheXpert classes (13 diseases plus the ‘No Finding’ label) with multi-label binary cross entropy loss. The 121-layer DenseNet was used as it produced the best results in prior studies [17, 18, 20, 23]. We followed identical procedures based on prior work for training CXR classification models [23]. Namely, all CXRs were center-cropped, resized to a resolution of 224×224 pixels, and normalized by the mean and standard deviation of the MIMIC-CXR train set. All classifiers were trained using AdamW optimizer with cosine scheduler (initial learning rate 0.0001, weight decay 0.05), for a maximum of 100 epochs; we early stopped if validation loss did not improve over 20 epochs.

Strategies for Initializing Model Weights We conducted a comprehensive comparison of how synthetic data can be used to train disease classifiers, evaluating four strategies: (i) Using only real CXRs; (ii) Using only synthetic CXRs generated by RoentGen-v2 ; (iii) Augmenting real CXRs with synthetic CXRs as is common in the literature; (iv) A two-stage training, where we first perform supervised pretraining with synthetic CXRs, followed by fine-tuning on real CXRs. In scenarios (i)–(iii) models were initialized using ImageNet pretrained weights; in scenario (iv) the model was trained from scratch. For models initialized with natural image (ImageNet) pretrained weights we used the available PyTorch weights. For the synthetic pretraining strategy, we trained the DenseNet121 from scratch on all the available synthetic images (initial learning rate 0.0001), and subsequently fine-tuned on real images (initial learning rate 0.00005). For each model, we saved the checkpoint with the highest average AUROC over 14 labels on the validation set.

4.5 Disease Classifier Evaluation Metrics

Classifier Performance To match the downstream disease classifiers that were trained only on PA images, we only used PA images in the test datasets. The only exception was VinDr, where all images were frontal views, but unspecified whether AP or PA. This may lead to reduced performance metrics on VinDr compared to the other datasets. We evaluated classification performance on the set of eight labels common across datasets: Atelectasis, Cardiomegaly, Consolidation, Edema, Effusion, Pneumonia, Pneumothorax, No Finding. We computed the area under the receiver-operating curve (AUROC) and area under the precision-recall curve (AUPRC). Since this was a multi-label classification problem, binary AUROC was computed for each label and values were then macro-averaged across the eight labels of interest; similar for average AUPRC. To obtain binarized predictions from the classifiers, we followed previous work in selecting the threshold that maximized the F1 score on the validation set [17, 18, 20]. This threshold optimization procedure was conducted separately for each model and label.

Fairness Metrics For fairness analysis, we considered intersectional subgroups defined by pairs of demographic attributes. For sex & race/ethnicity, the groups were: Asian males, Asian females, Black males, Black females, Hispanic males, Hispanic females, White males, and White females. For sex & age, we defined age categories for both men and women: 18-40, 40-60, 60-80, and over 80 years old. Supplementary Table 3 details the subgroup composition of each dataset.

The first fairness metric we considered was AUROC parity, following prior work [27]. To compute this metric, we first calculated the average AUROC within each demographic subgroup. The fairness gap was then defined as the absolute difference in AUROC between the highest- and lowest-performing subgroups.

Second, to assess model decision biases in underdiagnosed patients, we compared underdiagnosis rates across subpopulations. Following [18, 20], we defined the underdiagnosis rate as the false positive rate (FPR) of the model prediction for the ‘No Finding’ label at the levels of the subgroup. We defined the underdiagnosis gap as the absolute difference in FPR between the best and worst-performing subgroups.

Statistical Analysis Continuous variables are reported as means with corresponding 95% confidence intervals (CIs), estimated via 1,000 bootstrap resamples. AUROC comparisons were conducted using the DeLong test, a nonparametric approach validated for evaluating differences between correlated receiver-operating characteristic curves [45]. Differences in AUPRC values were assessed using a permutation test, a nonparametric method suitable for evaluating performance metrics without distributional assumptions [46]. Significance testing was performed with a type I error rate of 0.05. All processing was performed in Python (version 3.10.12), using the libraries numpy (version 1.25.2), scipy (version 1.16.1), pandas (version 2.3.0) and torchmetrics (version 1.7.3).

Data Availability

The main data supporting the results in this study are available within the article and its Supplementary Information. The MIMIC-CXR dataset (version 2.0.0) is available on PhysioNet after a credentialing process (<https://doi.org/10.13026/C2JT1Q>). The CheXpert Plus dataset is available from Stanford AIMI (<https://aimi.stanford.edu/datasets/chexpert-plus>). The NIH Chest X-rays dataset is available from Kaggle (<https://www.kaggle.com/datasets/nih-chest-xrays/data>). The PadChest dataset is available from BIMCV Medical Imaging Databank of the Valencia Region (<https://bimcv.cipf.es/bimcv-projects/padchest/>). The VinDr-CXR dataset (version 1.0.0) is available on PhysioNet after a credentialing process (<https://doi.org/10.13026/3akn-b287>). Links to access the code, model weights, and synthetic dataset generated during this study are available at <https://github.com/StanfordMIMI/RoentGen-v2>.

Acknowledgments

A.S.C. receives research support from NIH grants R01 HL167974, R01 HL169345, R01 AR077604, R01 EB002524, R01 AR079431, P41 EB027060; Advanced Research Projects Agency for Health (ARPA-H) contracts AY2AX000045 and 1AYSAX0000024-01; and the Medical Imaging and Data Resource Center (MIDRC), which is funded by the National Institute of Biomedical Imaging and Bioengineering (NIBIB) under contract 75N92020C00021 and through ARPA-H. J.J. acknowledges co-funding by EU from EuroHPC Joint Undertaking programm under grant no. 101182737 (MINERVA) as well as co-funding by the Federal Ministry of Education and Research of Germany (BMBF) under the grant 16HPC117K (MINERVA), funding under grant no. 01IS24085C (OPENHAFM), and under the grant no. 01IS22094B (WestAI - AI Service Center West). We gratefully acknowledge the Gauss Centre for Supercomputing e.V. for funding this work by providing computing time through the John von Neumann Institute for Computing (NIC) on the supercomputer JUWELS Booster at Jülich Supercomputing Centre (JSC), storage resources on JUST granted and operated by JSC and supported by Helmholtz Data Federation (HDF) and computing time granted by the JARA and JSC on the supercomputer JURECA at JSC.

Author Contributions

S.L.M. and A.S.C. conceived and co-led the project and drafted the initial paper. S.L.M., C.B. and P.C. trained RoentGen-v2 for CXR generation. S.L.M. and C.B. trained and evaluated the supervised disease classifiers. S.L.M. designed, implemented and conducted the experiments pertaining to synthetic data generation, pretraining with synthetic data, and fairness analysis. B.P. and J.G. helped with demographic based classifiers. J.B.D. and M.P. provided additional technical advice and assistance. M.C. and J.J. provided engineering and computational support. C.B., P.C., J.B.D., M.P., J.G., C.P.L. and A.S.C. helped revise the paper. A.S.C. supervised the project. C.P.L. and A.S.C. provided financial support for the project.

References

- [1] Yasmeena Akhter, Richa Singh, and Mayank Vatsa. Ai-based radiodiagnosis using chest x-rays: A review. *Frontiers in Big Data*, 6, April 2023.
- [2] Lisa Iyeke, Rachel Moss, Rochelle Hall, Jeffrey Wang, Laiba Sandhu, Brendan Appold, Enessa Kalontar, Demetra Menoudakos, Mityanand Ramnarine, Sean P LaVine, Seungjun Ahn, and Mark Richman. Reducing unnecessary ‘admission’ chest x-rays: An initiative to minimize low-value care. *Cureus*, October 2022.
- [3] Erdi Calli, Ecem Sogancioglu, Bram van Ginneken, Kicky G. van Leeuwen, and Keelin Murphy. Deep learning for chest x-ray analysis: A survey. *Medical Image Analysis*, 72:102125, August 2021.
- [4] Ekin Tiu, Ellie Talius, Pujan Patel, Curtis P. Langlotz, Andrew Y. Ng, and Pranav Rajpurkar. Expert-level detection of pathologies from unannotated chest x-ray images via self-supervised learning. *Nature Biomedical Engineering*, 6(12):1399–1406, September 2022.
- [5] Adnane Ait Nasser and Moulay A. Akhloufi. A review of recent advances in deep learning models for chest disease detection using radiography. *Diagnostics*, 13(1):159, January 2023.
- [6] Minki Kim, Ki-Ryum Moon, and Byoung-Dai Lee. Unsupervised anomaly detection for posteroanterior chest x-rays using multiresolution patch-based self-supervised learning. *Scientific Reports*, 13(1), February 2023.
- [7] Chihcheng Hsieh, Isabel Blanco Nobre, Sandra Costa Sousa, Chun Ouyang, Margot Brereton, Jacinto C. Nascimento, Joaquim Jorge, and Catarina Moreira. Mdf-net for abnormality detection by fusing x-rays with clinical data. *Scientific Reports*, 13(1), September 2023.
- [8] Ivo Baltruschat, Leonhard Steinmeister, Hannes Nickisch, Axel Saalbach, Michael Grass, Gerhard Adam, Tobias Knopp, and Harald Ittrich. Smart chest x-ray worklist prioritization using artificial intelligence: a clinical workflow simulation. *European Radiology*, 31(6):3837–3845, November 2020.
- [9] Benedikt Boecking, Naoto Usuyama, Shruthi Bannur, Daniel C. Castro, Anton Schwaighofer, Stephanie Hyland, Maria Wetscherek, Tristan Naumann, Aditya Nori, Javier Alvarez-Valle, Hoifung Poon, and Ozan Oktay. *Making the Most of Text Semantics to Improve Biomedical Vision–Language Processing*, page 1–21. Springer Nature Switzerland, 2022.
- [10] Shruthi Bannur, Stephanie Hyland, Qianchu Liu, Fernando Pérez-García, Maximilian Ilse, Daniel C. Castro, Benedikt Boecking, Harshita Sharma, Kenza Bouzid, Anja Thieme, Anton Schwaighofer, Maria Wetscherek, Matthew P. Lungren, Aditya Nori, Javier Alvarez-Valle, and Ozan Oktay. Learning to exploit temporal structure for biomedical vision-language processing, 2023.
- [11] Guanxiong Liu, Tzu-Ming Harry Hsu, Matthew McDermott, Willie Boag, Wei-Hung Weng, Peter Szolovits, and Marzyeh Ghassemi. Clinically accurate chest x-ray report generation, 2019.
- [12] Zhihong Chen, Maya Varma, Justin Xu, Magdalini Paschali, Dave Van Veen, Andrew Johnston, Alaa Youssef, Louis Blankemeier, Christian Bluethgen, Stephan Altmayer, Jeya Maria Jose Valanarasu, Mohamed Siddig Eltayeb Muneer, Eduardo Pontes Reis, Joseph Paul Cohen, Cameron Olsen, Tanishq Mathew Abraham, Emily B. Tsai, Christopher F. Beaulieu, Jenia Jitsev, Sergios Gatidis, Jean-Benoit Delbrouck, Akshay S. Chaudhari, and Curtis P. Langlotz. A vision-language foundation model to enhance efficiency of chest x-ray interpretation, 2024.
- [13] Ryutaro Tanno, David G. T. Barrett, Andrew Sellergren, Sumedh Ghaisas, Sumanth Dathathri, Abigail See, Johannes Welbl, Charles Lau, Tao Tu, Shekoofeh Azizi, Karan Singhal, Mike Schaeckermann, Rhys May, Roy Lee, SiWai Man, Sara Mahdavi, Zahra Ahmed, Yossi Matias, Joelle Barral, S. M. Ali Eslami, Danielle Belgrave, Yun Liu, Sreenivasa Raju Kalidindi, Shravya Shetty, Vivek Natarajan, Pushmeet Kohli, Po-Sen Huang, Alan Karthikesalingam, and Ira Ktena. Collaboration between clinicians and vision–language models in radiology report generation. *Nature Medicine*, 31(2):599–608, November 2024.

- [14] M.E. Milam and C.W. Koo. The current status and future of fda-approved artificial intelligence tools in chest radiology in the united states. *Clinical Radiology*, 78(2):115–122, February 2023.
- [15] Joseph Paul Cohen, Mohammad Hashir, Rupert Brooks, and Hadrien Bertrand. On the limits of cross-domain generalization in automated x-ray prediction, 2020.
- [16] Pablo Menéndez Fernández-Miranda, Enrique Marqués Fraguera, Marta Álvarez de Linera-Alperi, Miriam Cobo, Amaia Pérez del Barrio, David Rodríguez González, José A. Vega, and Lara Lloret Iglesias. A retrospective study of deep learning generalization across two centers and multiple models of x-ray devices using covid-19 chest-x rays. *Scientific Reports*, 14(1), June 2024.
- [17] Laleh Seyyed-Kalantari, Guanxiong Liu, Matthew McDermott, Irene Y. Chen, and Marzyeh Ghassemi. Chexclusion: Fairness gaps in deep chest x-ray classifiers, 2020.
- [18] Laleh Seyyed-Kalantari, Haoran Zhang, Matthew B. A. McDermott, Irene Y. Chen, and Marzyeh Ghassemi. Underdiagnosis bias of artificial intelligence algorithms applied to chest radiographs in under-served patient populations. *Nature Medicine*, 27(12):2176–2182, December 2021.
- [19] Monish Ahluwalia, Mohamed Abdalla, James Sanayei, Laleh Seyyed-Kalantari, Mohannad Hussain, Amna Ali, and Benjamin Fine. The subgroup imperative: Chest radiograph classifier generalization gaps in patient, setting, and pathology subgroups. *Radiology: Artificial Intelligence*, 5(5), September 2023.
- [20] Yuzhe Yang, Haoran Zhang, Judy W. Gichoya, Dina Katabi, and Marzyeh Ghassemi. The limits of fair medical imaging ai in real-world generalization. *Nature Medicine*, 30(10):2838–2848, June 2024.
- [21] Gustav Müller-Franzes, Jan Moritz Niehues, Firas Khader, Soroosh Tayebi Arasteh, Christoph Haarbuerger, Christiane Kuhl, Tianci Wang, Tianyu Han, Teresa Nolte, Sven Nebelung, Jakob Nikolas Kather, and Daniel Truhn. A multimodal comparison of latent denoising diffusion probabilistic models and generative adversarial networks for medical image synthesis. *Scientific Reports*, 13(1), July 2023.
- [22] Firas Khader, Gustav Müller-Franzes, Soroosh Tayebi Arasteh, Tianyu Han, Christoph Haarbuerger, Maximilian Schulze-Hagen, Philipp Schad, Sandy Engelhardt, Bettina Baeßler, Sebastian Foersch, Johannes Stegmaier, Christiane Kuhl, Sven Nebelung, Jakob Nikolas Kather, and Daniel Truhn. Denoising diffusion probabilistic models for 3d medical image generation. *Scientific Reports*, 13(1), May 2023.
- [23] Christian Bluethgen, Pierre Chambon, Jean-Benoit Delbrouck, Rogier van der Sluijs, Małgorzata Połacin, Juan Manuel Zambrano Chaves, Tanishq Mathew Abraham, Shivanshu Purohit, Curtis P. Langlotz, and Akshay S. Chaudhari. A vision–language foundation model for the generation of realistic chest x-ray images. *Nature Biomedical Engineering*, August 2024.
- [24] Tobias Weber, Michael Ingrisich, Bernd Bischl, and David Rügamer. Cascaded latent diffusion models for high-resolution chest x-ray synthesis, 2023.
- [25] Judy Wawira Gichoya, Imon Banerjee, Ananth Reddy Bhimireddy, John L Burns, Leo Anthony Celi, Li-Ching Chen, Ramon Correa, Natalie Dullerud, Marzyeh Ghassemi, Shih-Cheng Huang, Po-Chih Kuo, Matthew P Lungren, Lyle J Palmer, Brandon J Price, Saptarshi Purkayastha, Ayis T Pyrros, Lauren Oakden-Rayner, Chima Okechukwu, Laleh Seyyed-Kalantari, Hari Trivedi, Ryan Wang, Zachary Zaiman, and Haoran Zhang. Ai recognition of patient race in medical imaging: a modelling study. *The Lancet Digital Health*, 4(6):e406–e414, June 2022.
- [26] Bardia Khosravi, Frank Li, Theo Dapamede, Pouria Rouzrokh, Cooper U. Gamble, Hari M. Trivedi, Cody C. Wyles, Andrew B. Sellergrén, Saptarshi Purkayastha, Bradley J. Erickson, and Judy W. Gichoya. Synthetically enhanced: unveiling synthetic data’s potential in medical imaging research. *eBioMedicine*, 104:105174, June 2024.
- [27] Ira Ktena, Olivia Wiles, Isabela Albuquerque, Sylvestre-Alvise Rebuffi, Ryutaro Tanno, Abhijit Guha Roy, Shekoofeh Azizi, Danielle Belgrave, Pushmeet Kohli, Taylan Cemgil, Alan Karthikesalingam, and Sven Gowal. Generative models improve fairness of medical classifiers under distribution shifts. *Nature Medicine*, 30(4):1166–1173, April 2024.

- [28] Alistair E. W. Johnson, Tom J. Pollard, Seth J. Berkowitz, Nathaniel R. Greenbaum, Matthew P. Lungren, Chih-ying Deng, Roger G. Mark, and Steven Horng. Mimic-cxr, a de-identified publicly available database of chest radiographs with free-text reports. *Scientific Data*, 6(1), December 2019.
- [29] Joseph Paul Cohen, Joseph D. Viviano, Paul Bertin, Paul Morrison, Parsa Torabian, Matteo Guarrera, Matthew P. Lungren, Akshay Chaudhari, Rupert Brooks, Mohammad Hashir, and Hadrien Bertrand. Torchxrayvision: A library of chest x-ray datasets and models. In *Proceedings of the Medical Imaging with Deep Learning (MIDL)*, 2022. <https://github.com/mlmed/torchxrayvision>, arXiv:2111.00595.
- [30] Jeremy Irvin, Pranav Rajpurkar, Michael Ko, Yifan Yu, Silviana Ciurea-Ilcus, Chris Chute, Henrik Marklund, Behzad Haghighi, Robyn Ball, Katie Shpanskaya, Jayne Seekins, David A. Mong, Safwan S. Halabi, Jesse K. Sandberg, Ricky Jones, David B. Larson, Curtis P. Langlotz, Bhavik N. Patel, Matthew P. Lungren, and Andrew Y. Ng. Chexpert: A large chest radiograph dataset with uncertainty labels and expert comparison, 2019.
- [31] Pierre Chambon, Jean-Benoit Delbrouck, Thomas Sounack, Shih-Cheng Huang, Zhihong Chen, Maya Varma, Steven QH Truong, Chu The Chuong, and Curtis P. Langlotz. Chexpert plus: Augmenting a large chest x-ray dataset with text radiology reports, patient demographics and additional image formats, 2024.
- [32] Xiaosong Wang, Yifan Peng, Le Lu, Zhiyong Lu, Mohammadhadi Bagheri, and Ronald M. Summers. Chestx-ray8: Hospital-scale chest x-ray database and benchmarks on weakly-supervised classification and localization of common thorax diseases. In *2017 IEEE Conference on Computer Vision and Pattern Recognition (CVPR)*, pages 3462–3471. IEEE, 2017. <http://dx.doi.org/10.1109/CVPR.2017.369>.
- [33] Aurelia Bustos, Antonio Pertusa, Jose-Maria Salinas, and Maria de la Iglesia-Vayá. Padchest: A large chest x-ray image dataset with multi-label annotated reports. *Medical Image Analysis*, 66:101797, December 2020.
- [34] Ha Q. Nguyen, Khanh Lam, Linh T. Le, Hieu H. Pham, Dat Q. Tran, Dung B. Nguyen, Dung D. Le, Chi M. Pham, Hang T. T. Tong, Diep H. Dinh, Cuong D. Do, Luu T. Doan, Cuong N. Nguyen, Binh T. Nguyen, Que V. Nguyen, Au D. Hoang, Hien N. Phan, Anh T. Nguyen, Phuong H. Ho, Dat T. Ngo, Nghia T. Nguyen, Nhan T. Nguyen, Minh Dao, and Van Vu. Vindr-cxr: An open dataset of chest x-rays with radiologist’s annotations. *Scientific Data*, 9(1), July 2022.
- [35] Jeremy Irvin, Pranav Rajpurkar, Michael Ko, Yifan Yu, Silviana Ciurea-Ilcus, Chris Chute, Henrik Marklund, Behzad Haghighi, Robyn Ball, and Katie Shpanskaya. Chexpert: A large chest radiograph dataset with uncertainty labels and expert comparison. In *Thirty-Third AAAI Conference on Artificial Intelligence (AAAI 2019)*, 2019.
- [36] Salman Ul Hassan Dar, Marvin Seyfarth, Isabelle Ayx, Theano Papavassiliu, Stefan O. Schoenberg, Robert Malte Siepmann, Fabian Christopher Laqua, Jannik Kahmann, Norbert Frey, Bettina Baeßler, Sebastian Foersch, Daniel Truhn, Jakob Nikolas Kather, and Sandy Engelhardt. Unconditional latent diffusion models memorize patient imaging data. *Nature Biomedical Engineering*, August 2025.
- [37] Alec Radford, Jong Wook Kim, Chris Hallacy, Aditya Ramesh, Gabriel Goh, Sandhini Agarwal, Girish Sastry, Amanda Askell, Pamela Mishkin, Jack Clark, Gretchen Krueger, and Ilya Sutskever. Learning transferable visual models from natural language supervision, 2021.
- [38] OpenAI, Josh Achiam, Steven Adler, and et al. Gpt-4 technical report, 2023.
- [39] Dave Van Veen, Cara Van Uden, Maayane Attias, Anuj Pareek, Christian Bluethgen, Malgorzata Polacin, Wah Chiu, Jean-Benoit Delbrouck, Juan Manuel Zambrano Chaves, Curtis P. Langlotz, Akshay S. Chaudhari, and John Pauly. Radadapt: Radiology report summarization via lightweight domain adaptation of large language models, 2023.

- [40] Dave Van Veen, Cara Van Uden, Louis Blankemeier, Jean-Benoit Delbrouck, Asad Aali, Christian Bluethgen, Anuj Pareek, Malgorzata Polacin, Eduardo Pontes Reis, Anna Seehofnerová, Nidhi Rohatgi, Poonam Hosamani, William Collins, Neera Ahuja, Curtis P. Langlotz, Jason Hom, Sergios Gatidis, John Pauly, and Akshay S. Chaudhari. Adapted large language models can outperform medical experts in clinical text summarization. *Nature Medicine*, 30(4):1134–1142, February 2024.
- [41] Robin Rombach, Andreas Blattmann, Dominik Lorenz, Patrick Esser, and Björn Ommer. High-resolution image synthesis with latent diffusion models, 2021.
- [42] Ben Glocker, Charles Jones, Mélanie Bernhardt, and Stefan Winzeck. Algorithmic encoding of protected characteristics in chest x-ray disease detection models. *eBioMedicine*, 89:104467, March 2023.
- [43] Martin Heusel, Hubert Ramsauer, Thomas Unterthiner, Bernhard Nessler, and Sepp Hochreiter. Gans trained by a two time-scale update rule converge to a local nash equilibrium. In *Proceedings of the 31st International Conference on Neural Information Processing Systems (NeurIPS 2017)*, pages 6629–6640, Long Beach, California, USA, 2017. Curran Associates, Inc.
- [44] Christian Szegedy, Vincent Vanhoucke, Sergey Ioffe, Jonathon Shlens, and Zbigniew Wojna. Rethinking the inception architecture for computer vision, 2015.
- [45] Elizabeth R. DeLong, David M. DeLong, and Daniel L. Clarke-Pearson. Comparing the areas under two or more correlated receiver operating characteristic curves: A nonparametric approach. *Biometrics*, 44(3):837, September 1988.
- [46] Michael D. Ernst. Permutation methods: A basis for exact inference. *Statistical Science*, 19(4), November 2004.

Supplementary Information

Supplementary Results 1: RoentGen-v2 Checkpoint Selection

To select the best generative model checkpoint we computed several metrics to measure the quality of synthetic images across three distinct axes: (a) alignment with the provided findings text and demographics from the prompt, (b) similarity of generated images to real images, and (c) diversity among synthetic images generated from the same text prompt. Supplementary Table 1 summarizes the synthetic image quality metrics at each model checkpoint.

(a) Text Prompt Alignment For each text prompt in the validation set we generated synthetic CXRs. To evaluate how well synthetic CXRs depicted radiological findings that were included in the prompt, a pretrained classification model trained on real images (torch XRV [29]) was used to predict disease labels for the synthetic images. Similarly, to evaluate how well synthetic CXRs depicted the demographic information from the prompt, separate XRV models, trained on real data, were used to predict sex, race and age. The disease labels and patient metadata of the original text prompt represented the ground truth labels for the respective tasks. We report area under the receiver-operating characteristic curve (AUROC) for the diseases, accuracy for sex and race, and root mean square error (RMSE) for age predictions. Since the XRV classifiers themselves are imperfect, we compute a reference baseline by evaluating the classifier performance on the real images from the validation set (see Supplementary Table 1, ‘real data’ row).

The checkpoints at 7.5k training steps (equivalent to 21 epochs) and 10k training steps (equivalent to 28 epochs) achieved the highest average disease AUROC (0.81 compared to 0.88 for the real data baseline). The original RoentGen [23] model achieved an average disease AUROC of 0.82 (see Supplementary Table 1, ‘RoentGen’ row), showing we maintain the disease fidelity while introducing metadata variables in the conditional image generation process. For demographic attributes, sex and race accuracy for synthetic images were 100% and 99% respectively. As a reference, the XRV sex and race accuracy in classifying the real images were 97% and 95% respectively. This demonstrates the sex and race attributes were represented accurately by RoentGen-v2. The more challenging task of age prediction also had accurate results, with only a slightly larger root mean square error (8.9 yrs) compared to the real data (7.1 yrs). We note that training past 15k optimization steps (equivalent to 43 epochs) led to decreased classification performance for disease, sex and race, likely due to model overfitting. Overall, we observe near-perfect accuracy for demographics instruction following along with disease instruction following on par with the original RoentGen model.

(b) Real–Synthetic Image Similarity We used Fréchet Inception Distance (FID) score to compare the distribution of generated images with the distribution of the real ground truth images [43]. Out of all model checkpoints, the 10k training steps (equivalent to 28 epochs) checkpoint achieved the lowest FID score (76.8), indicating the most “realistic” image distribution. By comparison, the FID score of images generated by RoentGen [23] was 96.1.

While we aim to minimize the distance between the two image distributions, having individual synthetic images being exact replicas of real samples would be sub-optimal. To check for such model overfitting, we computed the image-level multi-scale structural similarity index (MS-SSIM) between generated images and their real counterparts, based on the same text prompt. We similarly computed the embedding-level similarity by measuring the cosine similarity of image embeddings, extracted using the image encoder of a domain-specific foundation model (BioViL [9]). In the case of MS-SSIM, the highest observed score was 0.41 at the 5k steps checkpoint (equivalent to 14 epochs), while the lowest observed score was 0.30 at 30k and 40k steps (equivalent to 86 and 115 epochs), with all other checkpoints scoring in-between. For the BioViL metric, the highest observed score was 0.52 at the 60k steps checkpoint (equivalent to 172 epochs), while the lowest observed score was 0.35 at 5k steps (equivalent to 14 epochs), with all other checkpoints scoring in-between. We observed balanced similarity scores (MS-SSIM and BioViL) between synthetic and original images for all model checkpoints, indicating we do not overfit to the real samples.

(c) Intra-prompt Diversity of Generated Images To measure the diversity of synthetic images generated by RoentGen-v2 , we generated multiple images using different random seeds for each text prompt in the validation set. We computed pairwise similarity scores (MS-SSIM and cosine similarity of BioViL embeddings) between images generated from the same prompt. For both metrics, a score of 1.00 would indicate that the model collapsed and is generating identical samples, thus lower scores are desirable. In the case of MS-SSIM, the highest observed score was 0.46 at the 5k steps checkpoint (equivalent to 14 epochs), while the lowest observed score was 0.24 at 30k and 40k steps (equivalent to 86 and 115 epochs), with all other checkpoints scoring in-between. For the BioViL metric, the highest observed score was 0.72 at the 5k steps checkpoint (equivalent to 14 epochs), while the lowest observed score was 0.52 at 20k steps (equivalent to 57 epochs), with all other checkpoints scoring in-between. Balanced intra-prompt similarity scores verify the ability of the model to generate distinct and varied images at multiple checkpoints.

Supplementary Tables

Supplementary Table 1: RoentGen-v2 checkpoints: synthetic image quality metrics.

| Checkpoint number of training steps (training epochs) | Text Prompt Alignment ² | | | | | Real-Synthetic Similarity ³ | | | | Intra-prompt Diversity ⁴ | | | | |
|--|------------------------------------|---------------|----------------|---------------|--------------|--|---------|--------|-----------|-------------------------------------|------|------|------|------|
| | Pneumothorax | | | | | FID ↓ | MS-SSIM | BioViL | MS-SSIM ↓ | BioViL ↓ | | | | |
| | Atelectasis | Cardiomegaly | Edema | Effusion | Pneumothorax | | | | | | | | | |
| | Average AUROC ↑ | Sex Acc. ↑ | Race Acc. ↑ | Age RMSE ↓ | | | | | | | | | | |
| real data | 0.75 | 0.83 | 0.92 | 0.81 | 0.92 | 0.88 | 0.97 | 0.95 | 7.1 | 0.0 | 1.00 | 1.00 | - | - |
| RoentGen | 0.80 | 0.86 | 0.81 | 0.93 | 0.72 | 0.82 | - | - | - | 96.1 | 0.36 | 0.59 | 0.42 | 0.77 |
| 5k (14 ep) | 0.72 | 0.81 | 0.84 | 0.73 | 0.87 | 0.79 | 1.00 | 0.98 | 9.4 | 77.2 | 0.41 | 0.35 | 0.46 | 0.72 |
| 7.5k (21 ep) | 0.78 | 0.81 | 0.84 | 0.72 | 0.93 | 0.81 | 1.00 | 0.99 | 8.7 | 81.9 | 0.39 | 0.36 | 0.39 | 0.73 |
| 10k (28 ep) | 0.76 | 0.77 | 0.82 | 0.78 | 0.90 | 0.81 | 1.00 | 0.98 | 8.9 | 76.8 | 0.37 | 0.41 | 0.37 | 0.66 |
| 12.5k (35 ep) | 0.74 | 0.83 | 0.80 | 0.73 | 0.89 | 0.80 | 1.00 | 0.98 | 7.9 | 86.4 | 0.37 | 0.43 | 0.36 | 0.62 |
| 15k (43 ep) | 0.76 | 0.80 | 0.79 | 0.73 | 0.89 | 0.80 | 0.99 | 0.98 | 8.4 | 87.4 | 0.34 | 0.44 | 0.31 | 0.57 |
| 20k (57 ep) | 0.75 | 0.77 | 0.72 | 0.70 | 0.89 | 0.76 | 0.97 | 0.95 | 8.5 | 103.5 | 0.31 | 0.47 | 0.26 | 0.52 |
| 30k (86 ep) | 0.70 | 0.78 | 0.71 | 0.66 | 0.89 | 0.75 | 0.98 | 0.96 | 8.7 | 101.3 | 0.30 | 0.48 | 0.24 | 0.54 |
| 40k (115 ep) | 0.69 | 0.80 | 0.72 | 0.64 | 0.89 | 0.75 | 0.97 | 0.94 | 8.8 | 99.2 | 0.30 | 0.49 | 0.24 | 0.56 |
| 50k (143 ep) | 0.72 | 0.81 | 0.73 | 0.65 | 0.90 | 0.76 | 0.98 | 0.95 | 8.9 | 97.9 | 0.31 | 0.51 | 0.26 | 0.60 |
| 60k (172 ep) | 0.72 | 0.81 | 0.74 | 0.65 | 0.91 | 0.77 | 0.98 | 0.96 | 8.8 | 90.9 | 0.32 | 0.52 | 0.28 | 0.60 |

¹Abbreviations: AUROC: area under the receiver-operating curve; FID: Fréchet Inception Distance, calculated using embeddings from an ImageNet-pretrained InceptionV3 network; MS-SSIM: multi-scale structural similarity index; BioViL: indicates cosine similarity between image embeddings obtained from BioViL image encoder.

²Text Prompt Alignment Metrics. For individual disease labels, showing binary AUROC. For sex and race, showing classification accuracy. For age, showing root mean square error (RMSE).

³Real-Synthetic Similarity Metrics. For FID, lower scores are better. For MS-SSIM and BioViL, higher scores indicate more resemblance to real images; however, a score of 1.00 would indicate model overfitting, i.e. synthetic samples identical to their real counterparts.

⁴Intra-prompt Diversity Metrics. Lower scores indicate more diversity; a score of 1.00 would indicate model collapse, i.e. always identical synthetic samples.

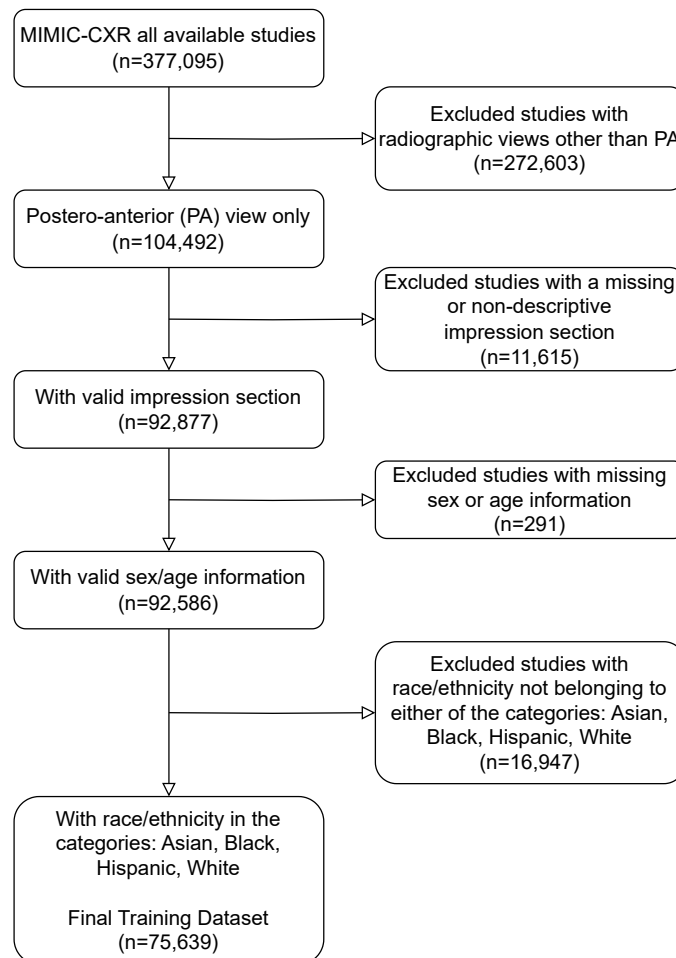
Supplementary Table 2: Description of chest radiography datasets.

| Subgroup | Attribute | MIMIC-CXR | | | | CheXpert | | NIH | | PadChest | | VinDr | |
|---------------------------------|---------------|----------------|-------------|---------------|--|----------------|--|----------------|--|----------------|--|---------------|--|
| | | train | val | test | | test | | test | | test | | test | |
| | Views | PA | PA | PA | | PA | | PA | | PA | | PA,AP | |
| Total | No.images | 66,760 | 1,295 | 7,584 | | 20,531 | | 47,075 | | 59,036 | | 3,000 | |
| Sex | Female | 32,593 (48.8%) | 514 (39.7%) | 3,670 (48.4%) | | 7,132 (34.7%) | | 20,872 (44.3%) | | 30,695 (52.0%) | | - | |
| | Male | 34,167 (51.2%) | 781 (60.3%) | 3,914 (51.6%) | | 13,399 (65.3%) | | 26,203 (55.7%) | | 28,341 (48.0%) | | - | |
| Age | 0-18 | - | - | - | | - | | 1,922 (4.1%) | | 1,789 (3.0%) | | - | |
| | 18-40 | 9,599 (14.4%) | 118 (9.1%) | 1,186 (15.6%) | | 3,622 (17.6%) | | 12,684 (26.9%) | | 5,614 (9.5%) | | - | |
| | 40-60 | 24,167 (36.2%) | 459 (35.4%) | 2,606 (34.4%) | | 7,179 (35.0%) | | 20,810 (44.2%) | | 16,666 (28.3%) | | - | |
| | 60-80 | 25,941 (38.8%) | 574 (44.3%) | 3,061 (40.4%) | | 7,722 (37.6%) | | 11,244 (23.9%) | | 22,682 (38.4%) | | - | |
| | 80+ | 7,053 (10.6%) | 144 (11.2%) | 731 (9.6%) | | 2,008 (9.8%) | | 415 (0.9%) | | 12,293 (20.8%) | | - | |
| | | | | | | | | | | | | | |
| Race/ Ethnicity ¹ | Asian | 2,452 (3.6%) | 14 (1.1%) | 299 (3.9%) | | 2,333 (11.4%) | | - | | - | | - | |
| | Black | 13,685 (20.5%) | 218 (16.8%) | 1,500 (19.8%) | | 1,174 (5.7%) | | - | | - | | - | |
| | Hispanic | 5,521 (8.3%) | 82 (6.3%) | 700 (9.2%) | | 2,401 (11.7%) | | - | | - | | - | |
| | White | 45,102 (67.6%) | 981 (75.8%) | 5,085 (67.1%) | | 11,395 (55.5%) | | - | | - | | - | |
| Target Diseases ² | No Finding | 34,028 (51.0%) | 472 (36.4%) | 3,783 (49.9%) | | 3,671 (17.9%) | | 27,379 (58.2%) | | 24,180 (41.0%) | | 2,051 (68.4%) | |
| | Atelectasis | 8,795 (13.2%) | 210 (16.2%) | 1,050 (13.8%) | | 4,531 (22.1%) | | 4,029 (8.6%) | | 2,477 (4.2%) | | 86 (2.9%) | |
| | Cardiomegaly | 7,074 (10.6%) | 173 (13.4%) | 831 (11.0%) | | 2,709 (13.2%) | | 1,122 (2.4%) | | 5,422 (9.2%) | | 309 (10.3%) | |
| | Consolidation | 2,209 (3.3%) | 83 (6.4%) | 209 (2.8%) | | 2,546 (12.4%) | | 1,059 (2.2%) | | 643 (1.1%) | | 96 (3.2%) | |
| | Edema | 4,332 (6.5%) | 142 (11.0%) | 504 (6.6%) | | 1,704 (8.3%) | | 181 (0.4%) | | 147 (0.3%) | | 0 (0.0%) | |
| | Effusion | 9,560 (14.3%) | 267 (20.6%) | 1,258 (16.6%) | | 6,542 (31.9%) | | 4,678 (9.9%) | | 2,032 (3.4%) | | 111 (3.7%) | |
| | Pneumonia | 8,806 (13.2%) | 247 (19.1%) | 976 (12.9%) | | 2,305 (11.2%) | | 438 (0.9%) | | 2,281 (3.9%) | | 246 (8.2%) | |
| | Pneumothorax | 1,696 (2.5%) | 31 (2.4%) | 197 (2.6%) | | 1,266 (6.2%) | | 2,386 (5.1%) | | 121 (0.2%) | | 18 (0.6%) | |
| | | | | | | | | | | | | | |
| | | | | | | | | | | | | | |

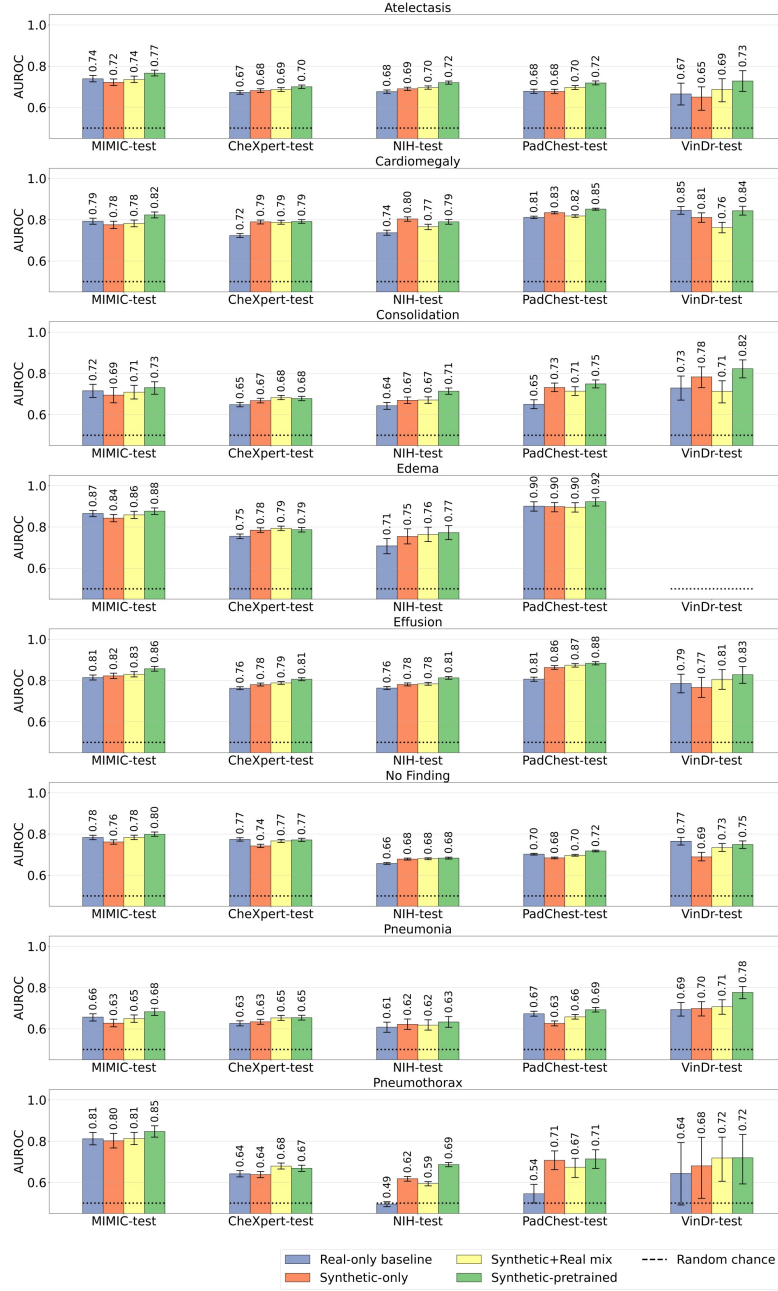
Supplementary Table 3: Description of demographic subgroup composition of chest radiography datasets.

| Intersectional Subgroup | MIMIC-CXR | | | CheXpert | NIH | PadChest |
|-------------------------|-----------|-------|-------|----------|--------|----------|
| | train | val | test | test | test | test |
| Total | 66,760 | 1,295 | 7,584 | 20,531 | 47,075 | 59,036 |
| White Male | 25,141 | 612 | 2,880 | 7,572 | - | - |
| White Female | 19,961 | 369 | 2,205 | 3,550 | - | - |
| Black Male | 5,366 | 105 | 576 | 653 | - | - |
| Black Female | 8,319 | 113 | 924 | 487 | - | - |
| Hispanic Male | 2,429 | 62 | 325 | 1,350 | - | - |
| Hispanic Female | 3,092 | 20 | 375 | 992 | - | - |
| Asian Male | 1,231 | 2 | 133 | 1,394 | - | - |
| Asian Female | 1,221 | 12 | 166 | 886 | - | - |
| Male aged under 18 | 0 | 0 | 0 | 0 | 1,071 | 933 |
| Female aged under 18 | 0 | 0 | 0 | 0 | 851 | 856 |
| Male aged 18 – 40 | 4,058 | 51 | 469 | 2,212 | 6,834 | 2,720 |
| Female aged 18 – 40 | 5,541 | 67 | 717 | 1,330 | 5,850 | 2,894 |
| Male aged 40 – 60 | 12,774 | 286 | 1,370 | 4,558 | 11,166 | 7,447 |
| Female aged 40 – 60 | 11,393 | 173 | 1,236 | 2,445 | 9,644 | 9,216 |
| Male aged 60 – 80 | 13,893 | 371 | 1,681 | 5,087 | 6,880 | 11,343 |
| Female aged 60 – 80 | 12,048 | 203 | 1,380 | 2,428 | 4,364 | 11,334 |
| Male aged over 80 | 3,442 | 73 | 394 | 1,230 | 252 | 5,898 |
| Female aged over 80 | 3,611 | 71 | 337 | 738 | 163 | 6,395 |

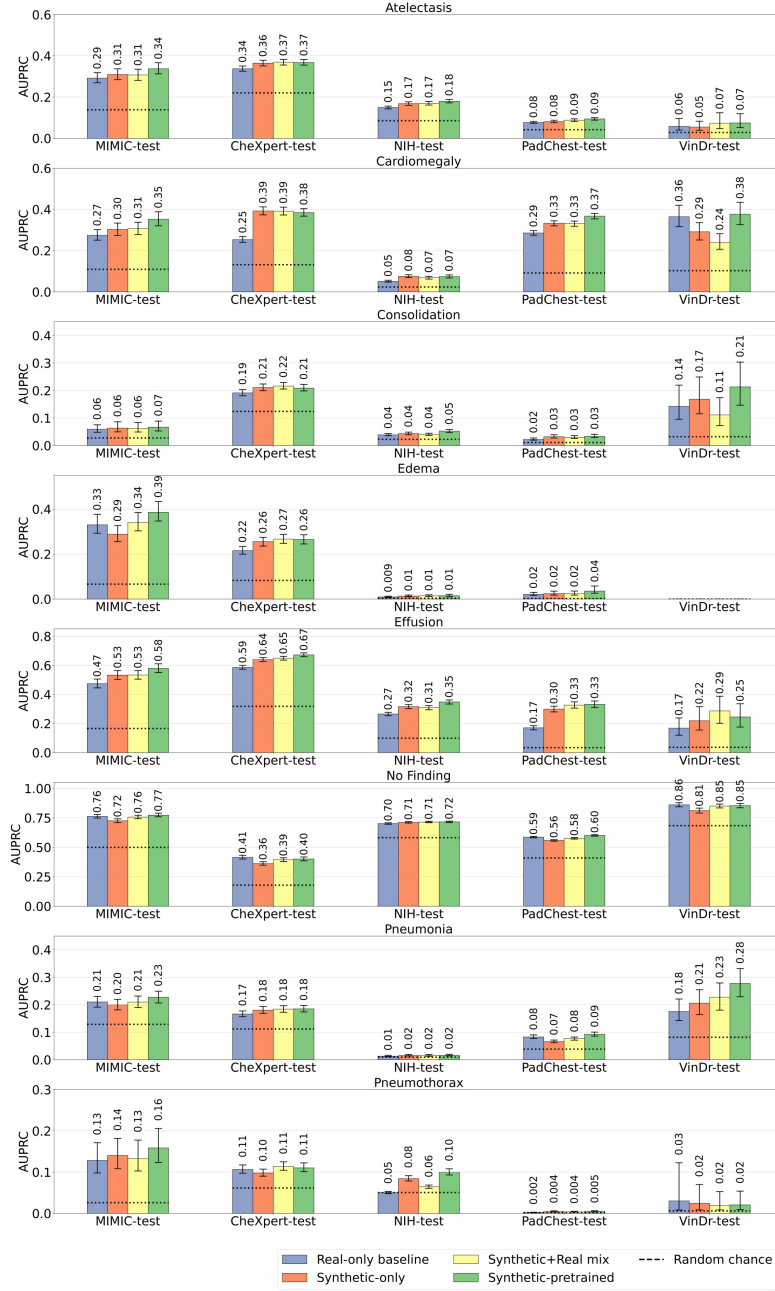
Supplementary Figures



Supplementary Figure 10: Selection criteria for the training dataset of the generative model.



Supplementary Figure 11: Classification performance of models trained on all available real and/or synthetic data according to four strategies: (i) Real-only (baseline) model trained on 66k real CXRs, (ii) Synthetic-only model trained on 565k synthetic CXRs, (iii) Synthetic+Real mix model trained on combined 66k real and 565k synthetic CXRs, and (iv) Synthetic-pretrained model, which underwent supervised pretraining on 565k synthetic CXRs followed by fine-tuning on 66k real CXRs. In scenarios (i)–(iii) models were initialized using ImageNet pretrained weights; in scenario (iv) the model was trained from scratch. Y-axis shows binary area under the receiver-operating curve (AUROC), with each panel focusing on one label. A random chance classifier would score 0.50 AUROC. For ‘Edema’ label, there are no patients with positive label in VinDr-test. Each model is evaluated in-distribution on MIMIC-test and out-of-distribution on four external datasets.



Supplementary Figure 12: Classification performance of models trained on all available real and/or synthetic data according to four strategies: (i) Real-only (baseline) model trained on 66k real CXRs, (ii) Synthetic-only model trained on 565k synthetic CXRs, (iii) Synthetic+Real mix model trained on combined 66k real and 565k synthetic CXRs, and (iv) Synthetic-pretrained model, which underwent supervised pretraining on 565k synthetic CXRs followed by fine-tuning on 66k real CXRs. In scenarios (i)–(iii) models were initialized using ImageNet pretrained weights; in scenario (iv) the model was trained from scratch. Y-axis shows binary area under the precision-recall curve (AUPRC), with each panel focusing on one label. A random chance classifier would score AUPRC equal to the label prevalence in the test dataset, hence the large differences in scores between labels and datasets. Each model is evaluated in-distribution on MIMIC-test and out-of-distribution on four external datasets. For ‘Edema’ label, there are no patients with positive label in VinDr-test; the disease prevalence is 0.004 in NIH-test, and 0.002 in PadChest-test. For ‘Pneumonia’ label, the disease prevalence in NIH-test is 0.009. For ‘Pneumothorax’ label, the disease prevalence is 0.002 in PadChest-test, and 0.006 in VinDr-test.

Supplementary Note 1: Disease-specific Classification Metrics

Supplementary Figure 11 shows the disease-specific AUROC metrics across all models and datasets. The trend observed in the macro-averaged multi-label AUROC was reflected in the binary classification AUROCs of individual imaging findings. Generally, the synthetic-pretrained model achieved the highest AUROC scores across datasets and diseases, with only a few exceptions. For Cardiomegaly on VinDr, there was no significant difference between the real-only baseline the synthetic-pretrained model (p-value= 0.80). For Consolidation on MIMIC, there was no significant difference between the real-only baseline the synthetic-pretrained model (p-value= 0.18). Lastly, for the No Finding label on CheXpert, there was no significant difference between the real-only baseline the synthetic-pretrained model (p-value= 0.43), and on VinDr the real-only model achieved higher AUROC than the synthetic-pretrained model (p-value= 0.02).

Supplementary Figure 12 shows the disease-specific AUPRC metrics across all models and datasets. Across the disease labels of Atelectasis, Cardiomegaly, Consolidation, Edema, Pleural Effusion, Pneumonia and Pneumothorax, the synthetic-pretrained model achieved the best binary AUPRC. For the ‘No Finding’ label, there was no significant difference between the proposed synthetic pretraining strategy and the baseline model.

Supplementary Note 2: Details of Pretrained CXR Classifiers

- Torch X-ray Vision library [29]: XRV version 1.3.5
- Disease classification model (XRV):
`xrv.models.DenseNet(weights="densenet121-res224-all")`
- Race classification model (XRV):
`xrv.baseline_models.emory_hiti.RaceModel()`
- Age prediction model (XRV):
`xrv.baseline_models.riken.AgeModel()`
- Sex classification model from [42]:
`SexModelResNet.load_from_checkpoint("sex_model_chexpert_resnet_all.ckpt")` with weights from <https://github.com/biomed-mira/chexploration/tree/main/prediction>
- Downstream disease classification models initialized with natural image (ImageNet) pretrained weights used the PyTorch weights
`DenseNet121_Weights.IMAGENET1K_V1`.